Int. J. Solids Structures Vol. 23, No. 7, pp. 841–869, 1987
Printed in Great Britain.

0020-7683/87 $3.00+ .00

STRAIN- AND STRESS-BASED CONTINUUM DAMAGE MODELS—II. COMPUTATIONAL ASPECTS

J. C. SIMO and J. W. JU
Department of Mechanical Engineering, Stanford University, Stanford, CA 94305, U.S.A.

(*Received* 4 *April* 1986; *in revised form* 8 *September* 1986)

Abstract—In Part I of this work we developed continuum isotropic and anisotropic elastoplastic-damage models, formulated either in strain space on the basis of the effective stress concept, or in stress space and employing the dual notion of effective strain. In Part II we consider in detail the variational formulation and subsequent numerical implementation of these models. The former relies crucially on the notions of maximum plastic and maximum damage dissipation. The latter makes systematic use of the operator splitting methodology to derive unconditionally stable algorithms for the numerical integration of the elastoplastic-damage equations of evolution. Appropriate extensions to treat the proposed rate-dependent (viscous) damage are also presented. For stress-based damage models, our numerical treatment relies on a new three-step operator split. The algorithms developed lead to simple and efficient stress update procedures suitable for large-scale finite element calculations. Application is made to a class of inviscid and rate-dependent cap models with an isotropic strain-based damage mechanism. Remarkably good agreement with existing experimental data that includes complicated stress paths is obtained. Numerical examples are also presented that demonstrate the good performance of the proposed algorithms.

1. INTRODUCTION

In Part I of this work, we developed alternative strain- and stress-based continuum damage models based on either the effective stress concept, or the effective strain concept. These formulations included both ductile and anisotropic brittle damage mechanisms. In Part II we consider in detail the computational aspects of the proposed damage models within the context of finite element methods. Two basic objectives are the development of a systematic and mathematically sound algorithmic treatment for this class of models, and the illustration of the effectiveness of this numerical treatment by means of numerical simulations. It will be shown that a significant advantage of the formulations developed in Part I lies in the simplicity of their numerical implementation that makes the proposed damage models ideally suited for large-scale computation. As a specific illustration, a rate-independent elastoplastic cap-damage model proposed in Part I is considered in detail. The remarkably good predictive capabilities of this simple phenomenological model will be demonstrated in a series of comparisons with available experimental data. Without loss of generality, in the developments that follow we shall neglect inertia effects and confine our attention to the static problem.

An outline of the paper is as follows. In Section 2 we develop the *variational* framework based on a displacement formulation in which only the equilibrium equation is enforced weakly.

In Section 3, the operator splitting methodology is systematically employed to develop unconditionally stable integration algorithms, for both strain- and stress-based models, that generalize return mapping algorithms for rate-independent plasticity and viscoplasticity[1–8]. (a) For the strain-based damage model, the resulting procedure takes the form of an *elastic-damage predictor/plastic corrector* scheme. An important difference between this procedure and the approach advocated in Ref. [2] is that the damage mechanism considered here is a *non-smooth* process which is accommodated in the algorithm in the *elastic-damage predictor* phase, not in the return mapping part of the algorithm. Computationally, this results in a *trivial modification* in the elastic predictor phase of existing rate-independent/rate-dependent algorithms to accommodate damage effects. (b) The methodology is immediately extended to include anisotropic damage. From a computational standpoint, the only change effects the elastic-damage predictor which now involves a local eigencalculation to compute the positive strain projection. (c) For the stress-based damage

model, on the other hand, we propose a *three-step* operator split that results in an *elastic predictor/plastic corrector/damage corrector* scheme. It is shown that for a completely general plastic response, with arbitrary yield condition and hardening law, the damage corrector merely reduces to the solution of a scalar non-linear equation. (d) As shown in Section 3.4, the methodology is readily extended to accommodate the rate-dependent viscous damage model developed in Secion 3.4 of Part I. We recall that this model results in well-posed, initial-value problems.

In Section 4 the algorithmic specialization of the proposed strain-based damage model to a cap plasticity model with isotropic damage for concrete is presented as an application of the proposed methodology. For convenience, a step-by-step account of the algorithmic details pertaining to the implementation of the proposed methodology have been collected in self-contained boxes. Finally, the predictive capabilities of the model and the performance of the algorithm are assessed by means of numerical simulations of available three-dimensional experimental data for concrete. These include uniaxial compression tests, complicated stress paths from the well-documented experimental effort at the University of Colorado[9], and several rate-dependent concrete tests.

2. VARIATIONAL FORMULATION OF THE ELASTOPLASTIC-DAMAGE MODEL

The variational formulation of the local form of the governing equations plays a central role in the numerical solution of the boundary value problem. In this section, we first develop a variational formulation for the strain-based damage model. By assuming that all of these conditions hold locally (point-wise) we recover the weak form of momentum balance. This latter form constitutes the basis of our subsequent algorithmic treatment.

2.1. *Variational framework*

Let us introduce the following space of kinematically admissible variations (virtual displacements):

$$V := \{\boldsymbol{\eta} : \Omega \to \mathbb{R}^N \,|\, \boldsymbol{\eta} \in [H^1(\Omega)]^N ; \boldsymbol{\eta}|_{\partial_u \Omega} = \mathbf{0}\} \tag{1}$$

where $N \leqslant 3$ is the spatial dimension, $H^1(\Omega)$ denotes the space of functions with derivatives bounded in energy, and $\partial_u \Omega \subset \partial\Omega$ is the part of $\partial\Omega$, the boundary of the body $\Omega \subset \mathbb{R}^N$, where the displacement field is specified as $\mathbf{u}|_{\partial_u \Omega} = \bar{\mathbf{u}}$. In addition, we let $\partial_\sigma \Omega \subset \partial\Omega$ be the part of the boundary where the stress vector is specified as $\boldsymbol{\sigma}\mathbf{n}|_{\partial_\sigma \Omega} = \bar{\mathbf{t}}$. With this notation at hand we introduce the functional

$$\Pi := \int_\Omega \{(1-d)\,[\Psi^0(\boldsymbol{\varepsilon}) - \boldsymbol{\varepsilon} : \bar{\boldsymbol{\sigma}}^p] + \boldsymbol{\sigma} : (\nabla^s \mathbf{u} - \boldsymbol{\varepsilon})\}\, d\Omega + \Pi_{\text{EXT}} \tag{2}$$

where

$$\Pi_{\text{EXT}} := -\int_\Omega \rho \mathbf{b} \cdot \mathbf{u}\, d\Omega - \int_{\partial_\sigma \Omega} \bar{\mathbf{t}} \cdot \mathbf{u}\, d\Gamma \tag{3}$$

represents the potential energy of the external loading. In eqn (2), $\Psi^0(\nabla^s \mathbf{u})$ denotes the (undamaged) initial elastic stored energy, and d is the damage parameter which is assumed to be a function of the history of strains $\boldsymbol{\varepsilon}$.

Remark 2.1. Functional (2) corresponds to a *Hu–Washizu* type of mixed variational form in which the local "strain–displacement" relations $\boldsymbol{\varepsilon} = \nabla^s \mathbf{u}$ are enforced *weakly* by means of the term

$$\int_\Omega \boldsymbol{\sigma} : [\nabla^s \mathbf{u} - \boldsymbol{\varepsilon}]\, d\Omega. \tag{4}$$

This generality is needed to provide a consistent variational framework for the so-called *assumed strain methods*[7,10]. The class of methods plays an essential role in treatment of constraints, such as incompressibility of the plastic flow. □

Remark 2.2. Note that we have selected $\bar{\sigma}^p$ and not σ^p as an independent variable. The motivation for this is found in the characterization of plastic response which, from the physical standpoint, is naturally formulated in terms of the effective plastic stress $\bar{\sigma}^p$. □

2.1.1. *Variational characterization of damage.* To develop a variational formulation of the *local* damage model proposed in Section 3 of Part I, we introduce the following "rate damage potential":

$$D^d := \int_\Omega [-\dot{\mu}\,\bar{g}(\Psi^0(\varepsilon), \bar{r}) + \dot{d}\Psi^0(\varepsilon)]\,d\Omega. \tag{5}$$

Here, $\dot{\mu}$ is a *damage consistency parameter* which in a local formulation is determined from the *damage consistency condition.* In the present variational context we assume that $\dot{\mu} \in K^d$ where K^d is the positive cone defined as

$$K^d := \{\dot{\mu} \mid \dot{\mu} \in L^2(\Omega), \qquad \dot{\mu} \geqslant 0\}. \tag{6}$$

In eqn (5) we have employed the notation $\bar{g}(\Psi^0, \bar{r}) := G(\sqrt{(2\Psi^0(\varepsilon))}) - \bar{r}$, where $G: \mathbb{R} \to \mathbb{R}_+$ is the damage potential introduced in Section 3.2 of Part I, a one-to-one monotonic function. In addition, $\dot{\bar{r}} := \dot{\mu} G'(\sqrt{(2\Psi^0)})/\sqrt{(2\Psi^0)}$ where a prime designates differentiation with respect to the argument. Finally, $\bar{r}$ is given by

$$\bar{r} := \int_0^t \dot{\bar{r}}\,ds. \tag{7}$$

Note that $\bar{g}(\Psi^0, \bar{r})$ coincides with $\bar{g}(\bar{\tau}, r)$ as defined in Remark 3.3 of Part I, simply by setting $\bar{r} = G(r)$.

2.1.2. *Variational characterization of plastic response.* A variational characterization of the evolution of the plastic flow defined by the *local* equations, eqns (19) of Part I, is accomplished by introducing the following "rate plastic potential" at current time $t \in \mathbb{R}_+$:

$$D^p := \int_\Omega \left[-\dot{\lambda} f\left(\frac{\partial \Psi^0(\varepsilon)}{\partial \varepsilon} - \bar{\sigma}^p, \mathbf{q}\right) + \boldsymbol{\varepsilon} : \dot{\bar{\sigma}}^p \right] d\Omega - \frac{d}{dt}\int_\Omega \Xi(\mathbf{q}, \bar{\sigma}^p)\,d\Omega. \tag{8}$$

Here, $\dot{\lambda} \in K^p$ is the "plastic consistency parameter" where K^p is the proper positive cone defined as

$$K^p := \{\dot{\lambda} \mid \dot{\lambda} \in L^2(\Omega); \qquad \dot{\lambda} \geqslant 0\}. \tag{9}$$

In expression (8) $\mathbf{q}$ is the vector of the internal plastic variables defined *locally* as

$$\dot{\mathbf{q}} = \dot{\lambda}\mathbf{h}(\sigma, \mathbf{q}), \qquad \dot{\lambda} \in K^p. \tag{10}$$

In addition, $\Xi(\mathbf{q})$ is the plastic potential function introduced in Section 3.1 of Part I, and $f(\partial\Psi^0(\varepsilon)/\partial\varepsilon - \bar{\sigma}^p, \mathbf{q}) = 0$ defines the plastic yield surface in *strain space* at time t.

A variational formulation of the equilibrium equations, strain–displacement relations, plastic flow and damage evolution rules, as well as plastic and damage consistency conditions may be obtained on the basis of the following functional

$$L := \Pi + \int_0^t [D^p + D^d]\,dt. \tag{11}$$

We refer to Simo and Honein[23] for further details.

Remark 2.3. It is entirely equivalent to use either $\Psi^0(\varepsilon)$ or the equivalent strain $\bar{\tau} := \sqrt{(2\Psi^0(\varepsilon))}$ as the basic independent variable. In what follows we revert to the notation of Part I, eqns (11)–(14), and employ $\bar{\tau}$ as an independent variable. □

2.1.3. *Displacement form.* By enforcing locally the plastic flow rule, the damage evolution equation, the plastic and damage loading/unloading conditions, as well as the damage and plastic dissipation inequalities, the above mixed variational forms collapse to the following single equation that provides the weak form of equilibrium

$$\bar{G}(\sigma, \eta) := \int_\Omega \sigma : \nabla^s \eta \, d\Omega + \bar{G}_{EXT} = 0 \tag{12a}$$

$$\bar{G}_{EXT} := -\int_\Omega \rho \mathbf{b} \cdot \eta \, d\Omega - \int_{\partial_\sigma \Omega} \bar{\mathbf{t}} \cdot \eta \, d\Gamma \tag{12b}$$

for any $\eta \in V$. The variational boundary value problem, eqns (12a) and (12b), is to be solved incrementally with the following *local* elastoplastic-damage rate constitutive equations appended

$$\begin{cases} \dot{\varepsilon} = \nabla^s \dot{\mathbf{u}}(t) \\ \dot{d}_t = \dot{\mu} H(\bar{\tau}_t) \\ \dot{r}_t = \dot{\mu} \\ \dot{\mu} \geqslant 0, \quad g(\bar{\tau}_t, r_t) \leqslant 0, \quad \dot{\mu} g(\bar{\tau}_t, r_t) = 0 \end{cases}$$

$$\dot{\bar{\sigma}} = \frac{d}{dt}\left[\frac{\partial \Psi^0(\varepsilon)}{\partial \varepsilon}\right] - \dot{\bar{\sigma}}^p \tag{13}$$

$$\begin{cases} \dot{\bar{\sigma}}^p = \dot{\lambda} \dfrac{\partial f}{\partial \varepsilon}\left(\dfrac{\partial \Psi^0(\varepsilon)}{\partial \varepsilon} - \bar{\sigma}^p, \mathbf{q}\right) \\ \dot{\mathbf{q}} = \dot{\lambda} \mathbf{h}\left(\dfrac{\partial \Psi^0(\varepsilon)}{\partial \varepsilon} - \bar{\sigma}^p, \mathbf{q}\right) \\ \dot{\lambda} \geqslant 0, \quad f(\bar{\sigma}, \mathbf{q}) \leqslant 0, \quad \dot{\lambda} f(\bar{\sigma}, \mathbf{q}) = 0 \end{cases}$$

where $\bar{\tau} := \sqrt{(2\Psi^0(\nabla^s \mathbf{u}))}$ is the equivalent strain.

2.1.4. *Numerical approximation scheme.* Within the context of finite element analysis, the numerical solution of eqns (12a) and (12b) is obtained by projecting onto a finite dimensional subspace $V^h \subset V$. A typical approximation scheme proceeds as follows. One considers a disjoint partition $\Omega \approx \bigcup_{e=1}^{N} \Omega_e$. Within a typical element, $\Omega_e \subset \Omega$, the displacements and displacement gradients are approximated as $\mathbf{u}|_{\Omega_e} = \mathbf{N}_e \mathbf{q}_e$ and $\nabla^s \mathbf{u}|_{\Omega_e} = \mathbf{B}_e \mathbf{q}_e$. Here, $\mathbf{q}_e$ is the vector of element nodal displacements, $\mathbf{N}$ is the vector of element shape functions and $\mathbf{B}_e$ is the *discrete gradient operator*. We note that in most currently employed successful finite element approximations $\mathbf{B}_e \neq \nabla \mathbf{N}$ (see, e.g. Ref. [7]). By assembly of the contribution of all the elements involved in the discretization one obtains the following expression at current time $t \in \mathbb{R}_+$ (inertia effects neglected)

$$\bar{G}(t) \approx \mathop{\mathsf{A}}_{e=1}^{N} \left\{ \delta \mathbf{q}_e^T \left[\int_\Omega \mathbf{B}_e^T \sigma(t)|_{\Omega_e} \, d\Omega \right] + \bar{G}_{EXT}|_{\Omega_e} \right\} = 0 \tag{14}$$

where A is the discrete assembly operator and, without loss of generality, inertia effects have been neglected. We note that eqn (14) is a function of the stresses $\sigma(t)$ (evaluated at Gauss points) which in turn, are defined in terms of the *history of strains* up to current time, $t \to \nabla^s \mathbf{u}(t)$, by *problem of evolution* (13). Thus, eqn (14) is transformed into a sequence of *non-linear algebraic problems* corresponding to discrete times $[t_0, t_1, t_2, \ldots] \subset \mathbb{R}_+$, by

numerically integrating problem (13). The development of such an algorithm is the objective of the following section.

3. ALGORITHMIC TREATMENT: OPERATOR SPLIT METHOD

In this section we address the problem of numerically integrating the elastoplastic-damage constitutive equations in the context of the finite element method. It is shown that by a systematic use of the operator splitting methodology a class of very efficient unconditionally stable algorithms can be developed for the two alternative formulations discussed in Part I of this work. In particular, the algorithmic treatment of the stress-based damage model relies on a new three-step operator split.

3.1. *Strain-based damage model*

From an algorithmic standpoint, the problem of integrating the evolution eqns (13) reduces to updating the basic variables $\{\boldsymbol{\sigma},\ d,\ \bar{\boldsymbol{\sigma}}^{\mathrm{p}},\ \mathbf{q}\}$ in a manner consistent with the constitutive model. It is essential to realize that in this computational process the history of strains $t \to \boldsymbol{\varepsilon} := \nabla^{\mathrm{s}}\mathbf{u}(t)$ is assumed to be given.

Equations of evolution (13) are to be solved incrementally over a sequence of given time steps $[t_n,\ t_{n+1}] \subset \mathbb{R}_+,\ n = 0, 1, 2, \ldots$. Thus, the initial conditions for eqns (13) are

$$\{\boldsymbol{\sigma}, d, \bar{\boldsymbol{\sigma}}^{\mathrm{p}}, \mathbf{q}\}|_{t=t_n} = \{\boldsymbol{\sigma}_n, d_n, \bar{\boldsymbol{\sigma}}^{\mathrm{p}}_n, \mathbf{q}_n\}. \tag{15}$$

In accordance with the notion of *operator split*, we consider the following *additive decomposition* of problem of evolution (13) into *elastic-damage* and *plastic* parts:

Elastic-damage part (16a)	*Plastic part* (16b)
$\dot{\boldsymbol{\varepsilon}} = \nabla^{\mathrm{s}}\dot{\mathbf{u}}(t)$	$\dot{\boldsymbol{\varepsilon}} = \mathbf{0}$
$\dot{d} = \begin{cases} H(\bar{\tau})\dot{\bar{\tau}} & \text{iff } g_t = \dot{g}_t = 0 \\ 0 & \text{otherwise} \end{cases}$	$\dot{d} = 0$
$\dot{r} = \begin{cases} \dot{\bar{\tau}} & \text{iff } g_t = \dot{g}_t = 0 \\ 0 & \text{otherwise} \end{cases}$	$\dot{r} = 0$
$\dot{\boldsymbol{\sigma}} = \dfrac{\mathrm{d}}{\mathrm{d}t}\left[\dfrac{\partial \Psi^0(\boldsymbol{\varepsilon})}{\partial \boldsymbol{\varepsilon}}\right]$	$\dot{\boldsymbol{\sigma}} = -\dot{\bar{\boldsymbol{\sigma}}}^{\mathrm{p}}$
$\dot{\bar{\boldsymbol{\sigma}}}^{\mathrm{p}} = \mathbf{0}$	$\dot{\bar{\boldsymbol{\sigma}}}^{\mathrm{p}} = \dot{\lambda}\dfrac{\partial f}{\partial \boldsymbol{\varepsilon}}\left(\dfrac{\partial \Psi^0(\boldsymbol{\varepsilon})}{\partial \boldsymbol{\varepsilon}} - \bar{\boldsymbol{\sigma}}^{\mathrm{p}}, \mathbf{q}\right)$
$\dot{\mathbf{q}} = \mathbf{0}$	$\dot{\mathbf{q}} = \dot{\lambda}\mathbf{h}\left(\dfrac{\partial \Psi^0(\boldsymbol{\varepsilon})}{\partial \boldsymbol{\varepsilon}} - \bar{\boldsymbol{\sigma}}^{\mathrm{p}}, \mathbf{q}\right).$

It is noted that both columns of eqns (16) do indeed add up to eqns (13) in agreement with the notion of operator split. The formulation of an algorithm consistent with eqns (13) is based on the following fundamental result concerning operator split methods[13]. Given two algorithms, the first one consistent with problem (16a) (*elastic-damage predictor*) and the second one consistent with problem (16b) (*return mapping corrector*), the product algorithm obtained by successive application of these two algorithms is consistent with the original problem (13).

3.1.1. *Elastic-damage predictor.* An algorithm consistent with problem (16a), referred to as the elastic-damage predictor in the sequel, is given by the following step-by-step procedure.

(i) *Strain update*: Given the incremental displacement field $\mathbf{u}_{n+1}$, the strain tensor is updated at Gauss points as

$$\varepsilon_{n+1} = \varepsilon_n + \nabla^s \mathbf{u}_{n+1}. \tag{17}$$

(ii) *Damage evolution*: One computes the equivalent strain $\bar{\tau}_{n+1}$ according to

$$\bar{\tau}_{n+1} := \sqrt{(2\Psi^0(\varepsilon_{n+1}))} \qquad (\textit{ductile}). \tag{18}$$

The damage variable d_{n+1} and the damage threshold r_{n+1} are then given by

$$d_{n+1} = \begin{cases} d_n & \text{if } \bar{\tau}_{n+1} - r_n \leqslant 0 \\ G(\bar{\tau}_{n+1}) & \text{otherwise} \end{cases} \tag{19}$$

$$r_{n+1} := \max\{r_n, \bar{\tau}_{n+1}\}. \tag{20}$$

(iii) *Trial (predictor) stress*: By mere substitution into the potential for the stress tensor we obtain

$$\begin{aligned} \boldsymbol{\sigma}^0_{n+1} &= \frac{\partial \Psi^0}{\partial \boldsymbol{\varepsilon}}(\boldsymbol{\varepsilon}_{n+1}) \\ \bar{\boldsymbol{\sigma}}^{\text{trial}}_{n+1} &= \boldsymbol{\sigma}^0_{n+1} - \bar{\boldsymbol{\sigma}}^{\text{p}}_n \\ \mathbf{q}^{\text{trial}}_{n+1} &= \mathbf{q}_n. \end{aligned} \tag{21}$$

We note that the elastic-damage predictor summarized above is not only consistent with (16a) but in fact furnishes the *exact solution* to this problem of evolution.

3.1.2. *Plastic return mapping corrector*. To develop an algorithm consistent with the plastic part (16b) of the operator split one first checks the *loading/unloading* conditions.

(iv) *Check for yielding and active mode*: The algorithmic counterpart of the Kuhn–Tucker conditions are trivially implemented in terms of the elastic-damage trial stress. One simply checks

$$f(\bar{\boldsymbol{\sigma}}^{\text{trial}}_{n+1}, \mathbf{q}^{\text{trial}}_{n+1}) \begin{cases} \leqslant 0 & \text{elastic-damage} \Rightarrow \text{predictor} \equiv \text{final state} \\ > 0 & \text{plastic} \Rightarrow \text{return mapping.} \end{cases} \tag{22}$$

Multi-surface plasticity: In the case of plastic loading, for multi-surface plasticity models it is necessary to determine the *active plastic surface*. As an example, for the cap model see Box 2.1.

(v) *Plastic return mapping corrector*: In the case of plastic loading the predictor stresses and internal variables are "returned back" to the yield surface along the algorithmic counterpart of the flow generated by (16b). The algorithmic construction of this flow follows a procedure proposed in Refs [2, 4], inspired in a form of Kelley's convex cutting plane method for non-linear optimization[14], with a basic structure inherited from Newton's method. Two fundamental advantages of this procedure are (a) the quadratic rate of convergence towards the yield surface and (b) the need for computing the gradient of the flow rule and hardening law is entirely by-passed.

Details pertaining to the application of the return mapping to the particular case of cap model are given in Box 2.2, and the generalization to the viscoplastic (rate-dependent) case is taken up in Box 3.1. A concise derivation of the cutting plane algorithm for the cap model is contained in the Appendix. The simplicity and efficiency of the overall procedure are noted.

3.2. *Extension to strain-based anisotropic brittle damage*

In Section 4.2.2 of Part I, we outlined the formulation of an anisotropic brittle damage model. The governing equations are given by eqns (53) of Part I. We show next that the methodology developed above can be immediately extended to accommodate anisotropic damage. Computationally, the only modification needed concerns the elastic-damage pre-

dictor, now involving an eigen-calculation to compute the positive projection of the strain tensor.

3.2.1. *Anisotropic elastic-damage predictor.* Steps (ii) and (iii) of the elastic-damage predictor outlined in Section 3.1.1 are modified as follows.

(ii) *Damage evolution*: Compute the equivalent strain $\bar{\tau}_{n+1}$ as follows.

(ii-1) Perform the spectral decomposition $\boldsymbol{\varepsilon}_{n+1} = \sum_{i=1}^{3} \varepsilon_i \mathbf{p}_i \otimes \mathbf{p}_i$.

(ii-2) Compute: $\boldsymbol{\varepsilon}^+ = \sum_{i=1}^{3} \bar{H}(\varepsilon_i)\varepsilon_i \mathbf{p}_i \otimes \mathbf{p}_i$ and $\mathbf{Q}^+ = \sum_{i=1}^{3} \bar{H}(\varepsilon_i)\mathbf{p}_i \otimes \mathbf{p}_i$.

(ii-3) Compute projection $\mathbf{P}^+ : P^+_{ijkl} = Q^+_{ia} Q^+_{jb} Q_{ka} Q_{lb}$.

(ii-4) Compute equivalent strain

$$\bar{\tau}_{n+1} := \sqrt{(\boldsymbol{\varepsilon}^+_{n+1} : \mathbf{C}^0 : \boldsymbol{\varepsilon}^+_{n+1})}. \tag{18'}$$

Recall that $\bar{H}(\cdot)$ denotes the Heaviside step function. The damage variable d_{n+1} and the damage threshold r_{n+1} are given by exactly the same expressions (19) and (20). In addition

$$\mathbf{C}_{n+1} = \begin{cases} \mathbf{C}_n & \text{if } \bar{\tau}_{n+1} - r_n \leqslant 0 \\ \mathbf{C}_n - (\bar{\tau}_{n+1} - \bar{\tau}_n) H(\bar{\tau}_{n+1}) \mathbf{P}^+_{n+1} \mathbf{C}^0 \mathbf{P}^+_{n+1} & \text{otherwise.} \end{cases} \tag{23}$$

(iii) *Trial (predictor) stress*: is computed by the same expressions (21). □

The rest of the algorithmic treatment, i.e. the plastic return mapping algorithm, is exactly the same one outlined previously in Section 3.1.2. It should be noted that all of the existing return mapping algorithms for elastoplasticity become applicable with no required modification in our proposed formulation and numerical treatment of elastoplastic-damage models.

Next, we turn our attention to the numerical solution of the stress-based isotropic damage model developed in Section 5 of Part I.

3.3. *Stress-based damage model*

From an algorithmic standpoint, the basic problem is again to formulate an update procedure for the state variables $\{\boldsymbol{\sigma}, d, \boldsymbol{\varepsilon}^p, \mathbf{q}\}$ which is consistent with the equations of evolution in Section 5 of Part I. Computationally, this process is strain driven in the sense that the history of strains $t \to \boldsymbol{\varepsilon} := \nabla^s \mathbf{u}(t)$ is assumed given. To develop such an update procedure, we propose the following *elastic–plastic–damage* operator split.

Elastic part (24a)	*Plastic part* (24b)	*Damage part* (24c)
$\dot{\boldsymbol{\varepsilon}} = \nabla^s \dot{\mathbf{u}}(t)$	$\dot{\boldsymbol{\varepsilon}} = \mathbf{0}$	$\dot{\boldsymbol{\varepsilon}} = \mathbf{0}$
$\dot{d} = 0$	$\dot{d} = 0$	$\dot{d} = \begin{cases} \dfrac{\partial G(\bar{\tau})}{\partial \bar{\tau}} \dot{\bar{\tau}} & \text{iff } g_t = \dot{g}_t = 0 \\ 0 & \text{otherwise} \end{cases}$
$\dot{r} = 0$	$\dot{r} = 0$	$\dot{r} = \begin{cases} \dot{\bar{\tau}} & \text{iff } g_t = \dot{g}_t = 0 \\ 0 & \text{otherwise} \end{cases}$
$\dot{\boldsymbol{\sigma}} = (1-d)\dfrac{\partial^2 \Psi^0}{\partial \boldsymbol{\varepsilon}^2} : \dot{\boldsymbol{\varepsilon}}$	$\dot{\boldsymbol{\sigma}} = -(1-d)\dfrac{\partial^2 \Psi^0}{\partial \boldsymbol{\varepsilon}^2} : \dot{\boldsymbol{\varepsilon}}^p$	$\dot{\boldsymbol{\sigma}} = -\dot{d}\dfrac{\partial^2 \Psi^0}{\partial \boldsymbol{\varepsilon}^2} : (\boldsymbol{\varepsilon} - \boldsymbol{\varepsilon}^p)$
$\dot{\boldsymbol{\varepsilon}}^p = \mathbf{0}$	$\dot{\boldsymbol{\varepsilon}}^p = \dot{\lambda}\dfrac{\partial f}{\partial \boldsymbol{\sigma}}(\boldsymbol{\sigma}, \mathbf{q})$	$\dot{\boldsymbol{\varepsilon}}^p = \mathbf{0}$
$\dot{\mathbf{q}} = \mathbf{0}$	$\dot{\mathbf{q}} = \dot{\lambda}\mathbf{h}(\boldsymbol{\sigma}, \mathbf{q})$	$\dot{\mathbf{q}} = \mathbf{0}$

We note again that the three columns of eqns (24) add up to the original problem of evolution, in accordance with the notion of operator split. The first two columns of eqns (24) define the classical elastoplastic problem, and the corresponding algorithmic treatment is based on the notion of elastic predictor/plastic return mapping corrector. Once the plastic consistency condition is enforced the state variables at the end of the plastic corrector phase become

$$\{\tilde{\boldsymbol{\sigma}}_{n+1}, \boldsymbol{\varepsilon}^{\mathrm{p}}_{n+1}, d_n, \mathbf{q}_{n+1}\}. \tag{25}$$

To complete the product formula algorithm consistent with eqns (24), it remains to develop an algorithm consistent with the damage part (24c) that operates on *initial conditions* (25) to produce the final state $\{\boldsymbol{\sigma}_{n+1}, \boldsymbol{\varepsilon}^{\mathrm{p}}_{n+1}, d_{n+1}, \mathbf{q}_{n+1}\}$.

3.3.1. *Damage corrector algorithm.* An integration procedure consistent with eqns (24c) proceeds along the following steps:

(i) *Check for damage-loading.* A trial "equivalent strain" $\tilde{\bar{\tau}}_{n+1}$ is computed from eqn (25) and the Kuhn–Tucker loading conditions checked so that

$$\text{IF } \tilde{\bar{\tau}}_{n+1} := \sqrt{(2\Lambda^0(\tilde{\boldsymbol{\sigma}}_{n+1}))} \leqslant r_n \Rightarrow \boldsymbol{\sigma}_{n+1} \equiv \tilde{\boldsymbol{\sigma}}_{n+1}, d_{n+1} \equiv d_n, \text{EXIT}. \tag{26}$$

If, on the other hand, condition (26) is violated then damage loading is taking place and eqns (24c) need to be solved.

(ii) *Damage return mapping* (if $\tilde{\bar{\tau}}_{n+1} := \sqrt{(2\Lambda^0(\tilde{\boldsymbol{\sigma}}_{n+1}))} > r_n$). The scalar nature of the damage leads to a particularly simple integration procedure. By damage consistency condition, $\dot{\mu} \equiv \dot{r}_t = \dot{\bar{\tau}}_t$. Hence eqns (24c) may be integrated by a backward-Euler difference scheme leading to

$$\begin{aligned} d_{n+1} &= G(\bar{\tau}_{n+1}) \\ \Delta\mu_{n+1} &= r_{n+1} - r_n \equiv \sqrt{(2\Lambda^0(\boldsymbol{\sigma}_{n+1}))} r_n \\ \boldsymbol{\sigma}_{n+1} &= \tilde{\boldsymbol{\sigma}}_{n+1} - \Delta\mu_{n+1} \frac{\partial G(\bar{\tau}_{n+1})}{\partial \bar{\tau}} \mathbf{C}^0 : (\boldsymbol{\varepsilon}_{n+1} - \boldsymbol{\varepsilon}^{\mathrm{p}}_{n+1}). \end{aligned} \tag{27}$$

Equations (27) may be solved by the simple Newton iterative scheme summarized in Box 1.

Box 1. Damage corrector iterative algorithm

(i) Initialize variables: $k = 0, \Delta\mu^{(0)}_{n+1} = 0, \boldsymbol{\sigma}^{(0)}_{n+1} = \tilde{\boldsymbol{\sigma}}_{n+1}$.

(ii) Compute stresses and "equivalent strain"

$$\boldsymbol{\sigma}^{(k)}_{n+1} = \tilde{\boldsymbol{\sigma}}_{n+1} - \Delta\mu^{(k)}_{n+1} \mathbf{C}^0 : (\boldsymbol{\varepsilon}_{n+1} - \boldsymbol{\varepsilon}^{\mathrm{p}}_{n+1})$$

$$\bar{\tau}^{(k)}_{n+1} := \sqrt{(2\Lambda^0(\boldsymbol{\sigma}^{(k)}_{n+1}))}$$

$$\beta_{n+1}(\Delta\mu^{(k)}_{n+1}) := \Delta\mu^{(k)}_{n+1} - \bar{\tau}^{(k)}_{n+1} + r_n$$

IF $\beta(\Delta\mu^{(k)}_{n+1}) < \text{tol}$, SET $d_{n+1} = G(\bar{\tau}^{(k)}_{n+1})$ and EXIT. ELSE:

(iii) Update damage consistency parameter

$$D\beta(\Delta\mu^{(k)}_{n+1}) := 1 + \frac{1}{\bar{\tau}^{(k)}_{n+1}} \nabla\Lambda^0(\boldsymbol{\sigma}^{(k)}_{n+1}) : \mathbf{C}^0 : (\boldsymbol{\varepsilon}_{n+1} - \boldsymbol{\varepsilon}^{\mathrm{p}}_{n+1})$$

$$\Delta\mu^{(k+1)}_{n+1} := \Delta\mu^{(k)}_{n+1} - \frac{\beta(\Delta\mu^{(k)}_{n+1})}{D\beta(\Delta\mu^{(k)}_{n+1})}$$

SET $k = k+1$ and GO TO (ii).

3.4. *Generalization to viscous strain-based damage*

A one parameter family of unconditionally stable integration algorithms for the incremental solution of the viscous damage model outlined in Section 3.4 of Part I is constructed as follows. Assume damage loading; that is, let $g(\bar{\tau}_{n+1}, r_n) := \bar{\tau}_{n+1} - r_n > 0$. Application of the generalized mid-point rule to eqns (29) of Part I then yields

$$\begin{aligned} d_{n+1} &= d_n + \Delta\mu\, g(\bar{\tau}_{n+\alpha}, r_{n+\alpha}) H(\bar{\tau}_{n+\alpha}) \\ r_{n+1} &= r_n + \Delta\mu\, g(\bar{\tau}_{n+\alpha}, r_{n+\alpha}) \equiv \Delta\mu(\bar{\tau}_{n+\alpha} - r_{n+\alpha}) \\ \bar{\tau}_{n+\alpha} &:= \sqrt{(2\Psi^0(\varepsilon_{n+\alpha}))}, \varepsilon_{n+\alpha} := \alpha\varepsilon_{n+1} + (1-\alpha)\varepsilon_n \\ r_{n+\alpha} &:= \alpha r_{n+1} + (1-\alpha) r_n \end{aligned} \tag{28}$$

where $\Delta\mu := \mu(t_{n+1} - t_n)$. The expansion experienced by the damage surface during the time step is determined from eqns (28) by solving for r_{n+1} to obtain

$$r_{n+1} = \frac{[1-(1-\alpha)\Delta\mu] r_n + \Delta\mu\bar{\tau}_{n+1}}{1+\alpha\Delta\mu}, \left(\alpha \geqslant \frac{1}{2}\right). \tag{29}$$

We recall from elementary numerical analysis that algorithm (28) and (29) is unconditionally stable for $(\alpha \geqslant 1/2)$ and second-order accurate for $\alpha = 1/2$. Typically, the value $\alpha = 1$ corresponding to a backward-Euler difference scheme is employed. We restrict our attention to this case in the ensuing discussion.

It is interesting to examine the limiting values $\mu \to 0$ and $\mu \to \infty$ of the damage fluidity coefficient, and their effect on the evolution of r_{n+1} and g_{n+1}.

(a) For $\mu \to 0$ (so that $\Delta\mu \to 0$), we obtain $r_{n+1} \to r_n$ and $g_{n+1} \to (\bar{\tau}_{n+1} - r_n)$. Hence, *no further damage* takes place during the time increment and (in the absence of plastic flow) one has *instantaneous elastic response*.

(b) For $\mu \to \infty$ (so that $\Delta\mu \to \infty$), we have that $r_{n+1} \to \bar{\tau}_{n+1}$, $g_{n+1} \to 0$, and $\Delta d_{n+1} = \Delta\bar{\tau}_{n+1} H(\bar{\tau}_{n+1})$. This situation corresponds to the rate-independent damage characterization discussed above. Hence, as $\mu \to \infty$ we recover the inviscid damage model characterized in Section 3.2 of Part I. Note that since $0 \leqslant \mu \leqslant \infty$ we must have $r_n \leqslant r_{n+1} \leqslant \bar{\tau}_{n+1}$; that is, the expansion of the damage surface is properly bounded between the instantaneous elasticity and the inviscid damage limit.

Remark 3.1. The damage behavior for extreme values of the fluidity coefficient μ is entirely analogous to that exhibited by viscoplastic models of the Perzyna type. We observe that the role of $\bar{\tau}$ in visco-damage is similar to that of σ in viscoplasticity. However, a fundamental difference is that $\bar{\tau}_{n+1}$ is computed directly in visco-damage models from the *given* strain ε_{n+1}, whereas in viscoplasticity σ_{n+1} needs to be computed by means of a *return mapping* algorithm. □

Remark 3.2. Equation $(29)_2$ in Section 3.4 of Part I, governing the evolution of r_t, is a first-order ordinary differential equation with exact solution in $[t_n, t_{n+1}]$ for given initial data. Explicitly, for visco-damage loading, at time $t \equiv t_{n+1}$ we have

$$\dot{r}_t + \mu r_t = \mu\bar{\tau}_t \tag{30}$$

along with the initial condition $r(t = t_n) = r_n$, at time $t \equiv t_n$. The solution at time t_{n+1} is

$$r_{n+1} = r_n + \int_{t_n}^{t_{n+1}} \mu \exp[-\mu(t_{n+1} - \xi)]\bar{\tau}_\xi \, d\xi. \tag{31}$$

Numerical integration is necessary since an explicit functional form for $\bar{\tau}_t$ in terms of t is not available in the general case. This motivates algorithm (28) and (29).

Box 1A. Visco-damage evolution algorithm

(i) Compute the current equivalent measure $\bar{\tau}_{n+1}$ according to

$$\bar{\tau}_{n+1} \equiv \sqrt{(2\Psi^0(\varepsilon_{n+1}))} \qquad \text{(ductile)}.$$

(ii) Check damage loading criterion: $g(\bar{\tau}_{n+1}, r_n) \equiv \bar{\tau}_{n+1} - r_n > 0$?

YES: visco-damage loading. Proceed to (iii).
No: no further damage. Exit.

(iii) Compute r_{n+1} and $\Delta\mu\, g(\bar{\tau}_{n+1}, r_{n+1})$:

$$\Delta\mu_{n+1} = \mu\Delta t_{n+1}$$

$$r_{n+1} = \frac{[r_n + \Delta\mu_{n+1}\bar{\tau}_{n+1}]}{[1+\Delta\mu_{n+1}]}$$

$$\Delta\mu\, g(\bar{\tau}_{n+1}, r_{n+1}) \equiv \Delta r_{n+1} = \frac{\Delta\mu_{n+1}}{1+\Delta\mu_{n+1}}(\bar{\tau}_{n+1} - r_n).$$

(iv) Update damage parameter:

$$\Delta d_{n+1} = \Delta\mu_{n+1}\, g_{n+1} H(\bar{\tau}^{\cdot}_{n+1})$$

$$d_{n+1} = d_n + \Delta d_{n+1}.$$

The integration scheme for visco-damage evolution is summarized for convenience in Box 1A for the full implicit case ($\alpha = 1$).

The remaining part of the numerical algorithm is the same as in Section 3.1. □

4. APPLICATION: CAP MODEL FOR CONCRETE INCLUDING DAMAGE

In this section we consider the application of the algorithmic framework developed in the previous sections to a specific constitutive model: the elastoplastic-damage cap model and the associated rate-dependent extension discussed in Part I of this work, eqns (73)–(79). See also Fig. 1. In what follows, we provide details on the strain-based algorithmic treatment by specializing the general algorithm outlined in Section 3.1. The visco-plastic (rate-dependent) extension of the proposed return mapping algorithm for the proposed cap-damage model is also considered. It will be shown that in spite of the simplicity of the cap-damage model outlined above, remarkably good agreement is obtained with well-documented experimental data for concrete. In particular, softening behavior is well captured.

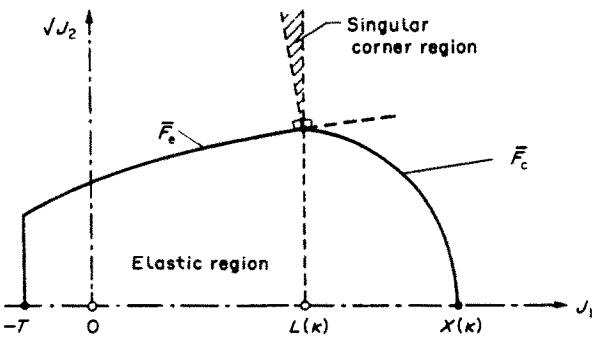

Fig. 1. The yield surface for the cap model. $\bar{F}_e$ and $\bar{F}_c$ denote the failure envelope and the hardening cap surface, respectively. The shaded area is the "singular corner region".

Box. 2.1. Specialization of proposed algorithm to cap model

(iii) Elastic-damage predictor:

$$\kappa_{n+1}^{\text{trial}} = \kappa_n$$

$$\bar{\mathbf{s}}_{n+1}^{\text{trial}} = \mathbf{s}_{n+1}^{0} - \bar{\mathbf{s}}_n^{\text{p}}$$

$$J_{1_{n+1}}^{0} := \operatorname{tr} \boldsymbol{\sigma}_{n+1}^{0}; \qquad \bar{J}_{1_n}^{\text{p}} := \operatorname{tr} \bar{\boldsymbol{\sigma}}_n^{\text{p}}$$

$$\bar{J}_{1_{n+1}}^{\text{trial}} = J_{1_{n+1}}^{0} - \bar{J}_{1_n}^{\text{p}}; \qquad \bar{J}_{2_{n+1}}^{\text{trial}} = \tfrac{1}{2}\bar{\mathbf{s}}_{n+1}^{\text{trial}} : \bar{\mathbf{s}}_{n+1}^{\text{trial}}.$$

(iv) Check for active mode (under yielding):

(a) *Tension cutoff mode*: if $\bar{J}_{1_{n+1}}^{\text{trial}} \leqslant T$, where $T :=$ tension cutoff.

$$\text{Set } \bar{J}_{1_{n+1}} = T; \qquad \sqrt{\bar{J}_{2_{n+1}}} = 0$$

$$\mathbf{s}_{n+1} = \mathbf{0}; \qquad \bar{\boldsymbol{\sigma}}_{n+1} = \tfrac{1}{3}\bar{J}_{1_{n+1}}\mathbf{1}; \qquad \boldsymbol{\sigma}_{n+1} = (1-d_{n+1})\bar{\boldsymbol{\sigma}}_{n+1}$$

$$\Delta\bar{\boldsymbol{\sigma}}_{n+1}^{\text{p}} = \bar{\boldsymbol{\sigma}}_{n+1}^{\text{trial}} - \bar{\boldsymbol{\sigma}}_{n+1}; \qquad \bar{\boldsymbol{\sigma}}_{n+1}^{\text{p}} = \bar{\boldsymbol{\sigma}}_n^{\text{p}} + \Delta\bar{\boldsymbol{\sigma}}_{n+1}^{\text{p}}; \qquad \text{EXIT.}$$

(b) *Cap mode*: if $\bar{J}_{1_{n+1}}^{\text{trial}} > L(\kappa_n)$. GO TO (v) in Box 2.2.

(c) *Failure/corner mode*: if $T < \bar{J}_{1_{n+1}}^{\text{trial}} \leqslant L(\kappa_n)$. GO TO (v) in Box 2.2.

Box 2.2. Plastic correction for cap model. Return mapping algorithm

(v) Plastic correction: for modes (b) and (c) in Box 2.1 (iv).

(a) *Initialization*: $i = 0$

$$\kappa_{n+1}^{(0)} = \kappa_{n+1}^{\text{trial}}; \qquad \bar{\boldsymbol{\sigma}}_{n+1}^{(0)} = \bar{\boldsymbol{\sigma}}_{n+1}^{\text{trial}}$$

$$\bar{J}_{1_{n+1}}^{(0)} = \bar{J}_{1_{n+1}}^{\text{trial}}; \qquad \sqrt{\bar{J}_{2_{n+1}}^{(0)}} = \sqrt{\bar{J}_{2_{n+1}}^{\text{trial}}}.$$

(b) *Convergence check*: (see also eqns (73) and (74) in Part I)

$$f_{n+1}^{(i)} := \bar{J}_{2_{n+1}}^{(i)} - \bar{F}(\bar{J}_{1_{n+1}}^{(i)}, \kappa_{n+1}^{(i)}) \leqslant \text{tol}?$$

Yes: Set $(\cdot)_{n+1} = (\cdot)_{n+1}^{(i)}$ and EXIT.
No: GO TO (c).

(c) *Computation* for $\Delta\kappa_{n+1}^{(i+1)}$ and $\Delta\lambda_{n+1}^{(i+1)}$:

$$\Delta\kappa_{n+1}^{(i+1)} = \left. \frac{f}{-\dfrac{\partial f}{\partial \kappa} - \dfrac{\dfrac{\partial f}{\partial \bar{\boldsymbol{\sigma}}} : \mathbf{C}^0 : \dfrac{\partial f}{\partial \bar{\boldsymbol{\sigma}}} h'(\kappa)}{3\bar{\Omega}}} \right|_{n+1}^{(i)}$$

$$\Delta\lambda_{n+1}^{(i+1)} = -\left. \frac{h'(\kappa)}{3\bar{\Omega}} \right|_{n+1}^{(i)} \Delta\kappa_{n+1}^{(i+1)}.$$

(d) Stress and hardening parameter update:

$$\kappa_{n+1}^{(i+1)} = \kappa_{n+1}^{(i)} + \Delta\kappa_{n+1}^{(i+1)}$$

$$\bar{\boldsymbol{\sigma}}_{n+1}^{\text{p}(i+1)} = \bar{\boldsymbol{\sigma}}_{n+1}^{\text{p}(i)} + \Delta\lambda_{n+1}^{(i+1)} \mathbf{C}^0 : \left. \frac{\partial f}{\partial \bar{\boldsymbol{\sigma}}} \right|_{n+1}^{(i)}; \qquad \bar{\boldsymbol{\sigma}}_{n+1}^{(i+1)} = \bar{\boldsymbol{\sigma}}_{n+1}^{(i)} - \Delta\bar{\boldsymbol{\sigma}}_{n+1}^{\text{p}(i+1)}$$

$$\bar{J}_{1_{n+1}}^{(i+1)} = \operatorname{tr} \bar{\boldsymbol{\sigma}}_{n+1}^{(i+1)}; \qquad \bar{J}_{2_{n+1}}^{(i+1)} = \tfrac{1}{2}\bar{\mathbf{s}}_{n+1}^{(i+1)} : \bar{\mathbf{s}}_{n+1}^{(i+1)}.$$

For cap mode: set $i = i+1$, GO TO (b).
For failure/corner mode: GO TO Box 2.3.

4.1. *Remarks on algorithmic implementation*

The numerical implementation of the cap-damage model proposed in Section 6.1 of Part I, eqns (73)–(77), is accomplished by specialization of the general return mapping algorithm summarized in Section 3.1 above. Details of this process may be found in Boxes 2.1–2.3. Due to the different functional forms of the cap surface and failure envelope, as well as the singularity at the intersection of these two surfaces, five alternative response modes must be considered when performing the plastic return mapping part. Following the recent treatment in Ref. [3], these modes are classified solely on the basis of the elastic-damage predictor, as indicated in Box 2.1. Note that for the sign convention tension is taken to be negative.

Details pertaining to the algorithmic implementation of the plastic return mapping algorithm for the cap model are contained in Box 2.2. Note that $\tilde{\Omega}$ in Box 2.2 is defined by eqn (A2) in the Appendix. As pointed out in Ref. [3], the singular corner region warrants a separate algorithmic treatment. The details have been summarized for convenience in Box 2.3. Note that our treatment of the corner region differs from that proposed in Ref. [15].

Remark 4.1. It is emphasized that the damage variable d remains *fixed* during the plastic return mapping, with value equal to that computed in the elastic-damage predictor phase. □

4.2. *Viscoplastic (rate-dependent) extension*

The operator splitting methodology developed in Section 3.1 can readily be extended to accommodate viscoplastic-damage response described by eqns (78) and (79) in Part I. The elastic-damage predictor remains as in the rate-independent case. The viscoplastic return mapping (corrector), on the other hand, requires modification since, in contrast with the inviscid case, complete relaxation towards the initial yield surface is not achieved at the end of the *given* time step $t \equiv t_{n+1}$. We proceed as follows.

Box. 2.3. Corner mode check for cap model

(v)-(e) Corner mode check: for failure/corner mode in Box 2.1 (iv)-(c).

(1) If $\bar{J}_{1_{n+1}}^{(i+1)} < \kappa_{n+1}^{(i+1)}$: failure mode.

Set $i = i+1$. GO TO (b) in Box 2.2.

(2) If $\bar{J}_{1_{n+1}}^{(i+1)} = \kappa_{n+1}^{(i+1)}$: corner mode. End of iteration process.

Set $\kappa_{n+1} = \kappa_{n+1}^{(i+1)}$; $\quad \bar{J}_{1_{n+1}} = \bar{J}_{1_{n+1}}^{(i+1)}$; $\quad \sqrt{\bar{J}_{2_{n+1}}} = F_e(\bar{J}_{1_{n+1}})$

$$\bar{\mathbf{s}}_{n+1} = \frac{\sqrt{\bar{J}_{2_{n+1}}}}{\sqrt{\bar{J}_{2_{n+1}}^{(i)}}}\,\bar{\mathbf{s}}_{n+1}^{(i)}; \qquad \bar{\boldsymbol{\sigma}}_{n+1} = \bar{\mathbf{s}}_{n+1} + \tfrac{1}{3}\bar{J}_{1_{n+1}}\mathbf{1}$$

$$\Delta\bar{\boldsymbol{\sigma}}_{n+1}^{p} = \bar{\boldsymbol{\sigma}}_{n+1}^{(i)} - \bar{\boldsymbol{\sigma}}_{n+1}; \qquad \bar{\boldsymbol{\sigma}}_{n+1}^{p} = \bar{\boldsymbol{\sigma}}_{n+1}^{p(i)} + \Delta\bar{\boldsymbol{\sigma}}_{n+1}^{p}; \text{EXIT.}$$

(3) If $\bar{J}_{1_{n+1}}^{(i+1)} > \kappa_{n+1}^{(i+1)}$: corner mode. Proceed as follows:

$$\eta := [\bar{J}_{1_{n+1}}^{(i)} - \kappa_{n+1}^{(i)}] \Big/ \left[\Delta\kappa_{n+1}^{(i+1)} + \Delta\lambda_{n+1}^{(i+1)}\,\mathrm{tr}\left(\mathbf{C}^0 : \frac{\partial f}{\partial \bar{\boldsymbol{\sigma}}}\right)_{n+1}^{(i)}\right]$$

$$\kappa_{n+1} = \kappa_{n+1}^{(i)} + \eta\Delta\kappa_{n+1}^{(i+1)} = \bar{J}_{1_{n+1}}; \qquad \sqrt{\bar{J}_{2_{n+1}}} = F_e(\bar{J}_{1_{n+1}})$$

$$\bar{\mathbf{s}}_{n+1} = \frac{\sqrt{\bar{J}_{2_{n+1}}}}{\sqrt{\bar{J}_{2_{n+1}}^{(i)}}}\,\bar{\mathbf{s}}_{n+1}^{(i)}; \qquad \bar{\boldsymbol{\sigma}}_{n+1} = \bar{\mathbf{s}}_{n+1} + \tfrac{1}{3}\bar{J}_{1_{n+1}}\mathbf{1}$$

$$\Delta\bar{\boldsymbol{\sigma}}_{n+1}^{p} = \bar{\boldsymbol{\sigma}}_{n+1}^{(i)} - \bar{\boldsymbol{\sigma}}_{n+1}; \qquad \bar{\boldsymbol{\sigma}}_{n+1}^{p} = \bar{\boldsymbol{\sigma}}_{n+1}^{p(i)} + \Delta\bar{\boldsymbol{\sigma}}_{n+1}^{p}; \qquad \text{EXIT.}$$

Recall that by application of the cutting plane return mapping procedure, the return path towards the loading surface is approximated by a sequence of straight segments. Within each segment the stress point spends a total amount of time $\Delta t_{n+1}^{(i+1)}$, which is *a priori unknown*. The relaxation process is completed when the following constraint condition is met

$$\sum_{i=1}^{\text{num. segments}} \Delta t_{n+1}^{(i)} = t_{n+1} - t_n. \tag{32}$$

Given $t_{n+1}^{(i)} < t_{n+1}$, one determines the subsequent $\Delta t_{n+1}^{(i+1)}$ as follows. Making use of the chain rule one has

$$\frac{\partial \phi}{\partial t} = \frac{\partial \phi}{\partial \bar{\boldsymbol{\sigma}}} : \dot{\bar{\boldsymbol{\sigma}}} + \frac{\partial \phi}{\partial \mathbf{q}} : \dot{\mathbf{q}}. \tag{33}$$

The rate of change of the viscous flow function $\phi(f)$ may then be expressed as

$$\frac{\partial \phi}{\partial t} = -\frac{\phi}{\bar{t}} \tag{34}$$

where

$$\bar{t} := \frac{1}{\frac{1}{\tau}\frac{\partial \phi}{\partial f}\left[\frac{\partial f}{\partial \bar{\boldsymbol{\sigma}}} : \mathbf{C}^0 : \frac{\partial f}{\partial \bar{\boldsymbol{\sigma}}} - \frac{\partial f}{\partial \mathbf{q}} \cdot \mathbf{h}\right]} \tag{35}$$

By integration of (34) we find that $\Delta t_{n+1}^{(i+1)}$ is given by

$$\Delta t_{n+1}^{(i+1)} = \bar{t}_{n+1}^{(i)} \ln \frac{\phi_{n+1}^{(i)}}{\phi_{n+1}^{(i+1)}}. \tag{36}$$

Once $\Delta t_{n+1}^{(i+1)}$ has been determined by eqn (36) the updated stress tensor $\boldsymbol{\sigma}_{n+1}^{(i+1)}$ and the updated internal variable vector $\mathbf{q}_{n+1}^{(i+1)}$ can be readily obtained. The procedure is summarized for convenience in Box 3.1 and is recursively applied until condition (32) is satisfied.

The singular corner region again warrants an independent treatment. From the viscous flow rule (78) of Part I and the formulation in Ref. [3], we have the following equations under loading condition:

$$\bar{\Omega} = \frac{G}{9K} \frac{\bar{J}_{1_{n+1}} - \bar{J}_{1_{n+1}}^{(i)}}{\sqrt{(\bar{J}_{2_{n+1}}^{(i)})} - F_e(\bar{J}_{1_{n+1}})}; \qquad \Delta \varepsilon_{v_{n+1}}^{vp} := \varepsilon_v^{vp}(\kappa_{n+1}) - \varepsilon_v^{vp}(\kappa_{n+1}^{(i)})$$

$$\bar{f}(\bar{\boldsymbol{\sigma}}_{n+1}, \kappa_{n+1}) := \sqrt{(\bar{J}_{2_{n+1}})} - F_e(\bar{J}_{1_{n+1}}); \qquad \phi(\bar{f})_{n+1} = -\left.\frac{\Delta \varepsilon_v^{vp}}{3\bar{\Omega}\Delta\lambda}\right|_{n+1} \tag{37}$$

$$\sqrt{\bar{J}_{2_{n+1}}} = \bar{f}_{n+1} + F_{e_{n+1}} \qquad (f > 0 \textit{ when loading})$$

where $\Delta\lambda := \Delta t/\tau$. Based on the equations a step-by-step update procedure is summarized in Box 3.2.

Remark 4.2. It is noted that as $\tau \to 0$, the rate-independent constitutive behavior is recovered. This is in agreement with the formulation of the consistency condition in the inviscid case by a penalty procedure. □

Box 3.1. Viscoplastic correction for cap model

(v) Viscoplastic correction: for modes (b) and (c) in Box 2.1 (iv).

(a) *Initialization*: $i = 0$

$$\kappa_{n+1}^{(0)} = \kappa_{n+1}^{\text{trial}}; \qquad \bar{\boldsymbol{\sigma}}_{n+1}^{(0)} = \bar{\boldsymbol{\sigma}}_{n+1}^{\text{trial}}$$

$$\bar{J}_{1_{n+1}}^{(0)} = \bar{J}_{1_{n+1}}^{\text{trial}}; \qquad \sqrt{\bar{J}_{2_{n+1}}^{(0)}} = \sqrt{\bar{J}_{2_{n+1}}^{\text{trial}}}.$$

(b) *Computation* of $\Delta\kappa_{n+1}^{(i+1)}, \Delta\gamma_{n+1}^{(i+1)} := \Delta t \phi_{n+1}^{(i+1)}/\tau$, and $\bar{t}_{n+1}^{(i)}$:

$$\bar{t}_{n+1}^{(i)} = \frac{\tau}{\dfrac{\partial \phi}{\partial f}\left\{\dfrac{\partial f}{\partial \kappa}\dfrac{3\bar{\Omega}}{h'} + \dfrac{\partial f}{\partial \bar{\boldsymbol{\sigma}}} : \mathbf{C}^0 : \dfrac{\partial f}{\partial \bar{\boldsymbol{\sigma}}}\right\}}\Bigg|_{n+1}^{(i)}$$

$$\Delta\gamma_{n+1}^{(i+1)} = \frac{f\bar{t}}{\tau}\Bigg|_{n+1}^{(i)}; \qquad \Delta\kappa_{n+1}^{(i+1)} := -\frac{3\bar{\Omega}}{h'}\Bigg|_{n+1}^{(i)} \Delta\gamma_{n+1}^{(i+1)}.$$

(c) Stress and hardening parameter, and time update:

$$\kappa_{n+1}^{(i+1)} = \kappa_{n+1}^{(i)} + \Delta\kappa_{n+1}^{(i+1)}; \qquad t_{n+1}^{(i+1)} = t_{n+1}^{(i)} + \bar{t}_{n+1}^{(i)} \ln \frac{\phi_{n+1}^{(i)}}{\phi_{n+1}^{(i+1)}}$$

$$\bar{\boldsymbol{\sigma}}_{n+1}^{\text{vp}(i+1)} = \bar{\boldsymbol{\sigma}}_{n+1}^{\text{vp}(i)} + \Delta\gamma_{n+1}^{(i+1)} \mathbf{C}^0 : \frac{\partial f}{\partial \bar{\boldsymbol{\sigma}}}\Bigg|_{n+1}^{(i)}; \qquad \bar{\boldsymbol{\sigma}}_{n+1}^{(i+1)} = \bar{\boldsymbol{\sigma}}_{n+1}^{(i)} - \Delta\bar{\boldsymbol{\sigma}}_{n+1}^{\text{vp}(i+1)}$$

$$\bar{J}_{1_{n+1}}^{(i+1)} = \operatorname{tr} \bar{\boldsymbol{\sigma}}_{n+1}^{(i+1)}; \qquad \bar{J}_{2_{n+1}}^{(i+1)} = \tfrac{1}{2}\bar{\mathbf{s}}_{n+1}^{(i+1)} : \bar{\mathbf{s}}_{n+1}^{(i+1)}.$$

(d) *Check* for end of relaxation process: $t_{n+1}^{(i+1)} \geqslant t_{n+1}$?

Yes: $\Delta\gamma_{n+1} = \Delta\gamma_{n+1}^{(i+1)}[1 - \exp(-(t_{n+1} - t_{n+1}^{(i)})/\bar{t}_{n+1}^{(i)})]$

$$\Delta\kappa_{n+1} = -\frac{3\bar{\Omega}}{h'}\Bigg|_{n+1}^{(i)} \Delta\gamma_{n+1}$$

$$\kappa_{n+1} = \kappa_{n+1}^{(i)} + \Delta\kappa_{n+1}$$

$$\bar{\boldsymbol{\sigma}}_{n+1}^{\text{vp}} = \bar{\boldsymbol{\sigma}}_{n+1}^{\text{vp}(i)} + \Delta\gamma_{n+1} \mathbf{C}^0 : \frac{\partial f}{\partial \bar{\boldsymbol{\sigma}}}\Bigg|_{n+1}^{(i)}; \qquad \bar{\boldsymbol{\sigma}}_{n+1} = \bar{\boldsymbol{\sigma}}_{n+1}^{(i)} - \Delta\bar{\boldsymbol{\sigma}}_{n+1}^{\text{vp}}$$

$$\bar{J}_{1_{n+1}} = \operatorname{tr} \bar{\boldsymbol{\sigma}}_{n+1}; \qquad \bar{J}_{2_{n+1}} = \tfrac{1}{2}\bar{\mathbf{s}}_{n+1} : \bar{\mathbf{s}}_{n+1}.$$

For cap mode: EXIT.
For failure/corner mode: GO TO Box 3.2.

No: For cap mode, set $i = i+1$, GO TO (b).
For failure/corner mode: GO TO Box 3.2.

4.3. *Numerical examples: inviscid case*

In Section 6.1 of Part I of this work, we summarized an elastoplastic cap-damage model for application primarily intended to concrete materials. Its algorithmic treatment has been examined in detail in the preceding sections. It remains to assess the ability of this simple constitutive model to reproduce, within bounds of experimental error, available testing data and to demonstrate the efficiency of the proposed algorithm in numerical computations.

In view of the present shortcomings of experimental techniques and the wide scattering in available experimental data for concrete, a precise quantitative evaluation of the predicting capabilities of a given constitutive model does not seem to be warranted. Instead, it is felt that an *overall qualitative* reproduction of the main features of material behavior

Box. 3.2. Corner mode check for visco-plastic cap model

(v)-(e) Corner mode check: for failure/corner mode in Box 2.1 (iv)-(c).

For end of relaxation: $\bar{J}_{1_{n+1}}^{(i+1)} \equiv \bar{J}_{1_{n+1}}, \kappa_{n+1}^{(i+1)} \equiv \kappa_{n+1}, \Delta\gamma_{n+1}^{(i+1)} \equiv \Delta\gamma_{n+1}$

(1) If $\bar{J}_{1_{n+1}}^{(i+1)} < \kappa_{n+1}^{(i+1)}$: failure mode.

If end relaxation: EXIT.
Otherwise: Set $i = i+1$. GO TO (b) in Box 3.1.

(2) If $\bar{J}_{1_{n+1}}^{(i+1)} = \kappa_{n+1}^{(i+1)}$: corner mode. Proceed as (v)-(e)-(2) in Box 2.3.

(3) If $\bar{J}_{1_{n+1}}^{(i+1)} > \kappa_{n+1}^{(i+1)}$: corner mode. Proceed as follows:

$$\eta := [\bar{J}_{1_{n+1}}^{(i)} + \kappa_{n+1}^{(i)}] \Big/ \left[\Delta\kappa_{n+1}^{(i+1)} + \Delta\gamma_{n+1}^{(i+1)} \operatorname{tr}\left(\mathbf{C}^0 : \frac{\partial f}{\partial \bar{\boldsymbol{\sigma}}}\Big)_{n+1}^{(i)} \right]$$

$$\kappa_{n+1} = \kappa_{n+1}^{(i)} + \eta\Delta\kappa_{n+1}^{(i+1)} = \bar{J}_{1_{n+1}}; \qquad \Delta\lambda_{n+1} := \frac{1}{\tau}[t_{n+1} - t_{n+1}^{(i)}]$$

$$\bar{\Omega} = \frac{G}{9K} \frac{\bar{J}_{1_{n+1}} - \bar{J}_{1_{n+1}}^{(i)}}{\sqrt{(\bar{J}_{2_{n+1}}^{(i)}) - F_e(\bar{J}_{1_{n+1}})}}; \qquad \Delta\varepsilon_{v_{n+1}}^{vp} := \varepsilon_v^{vp}(\kappa_{n+1}) - \varepsilon_v^{vp}(\kappa_{n+1}^{(i)})$$

$$\phi(\bar{J})_{n+1} = -\frac{\Delta\varepsilon_{v_{n+1}}^{vp}}{3\bar{\Omega}\Delta\lambda}\Big|_{n+1}; \qquad \sqrt{\bar{J}_{2_{n+1}}} = F_e(\bar{J}_{1_{n+1}}) + \bar{J}_{n+1}$$

$$\bar{\mathbf{s}}_{n+1} = \frac{\sqrt{\bar{J}_{2_{n+1}}}}{\sqrt{\bar{J}_{2_{n+1}}^{(i)}}} \bar{\mathbf{s}}_{n+1}^{(i)}; \qquad \bar{\boldsymbol{\sigma}}_{n+1} = \bar{\mathbf{s}}_{n+1} + \tfrac{1}{3}\bar{J}_{1_{n+1}}\mathbf{1}$$

$$\Delta\bar{\boldsymbol{\sigma}}_{n+1}^{vp} = \bar{\boldsymbol{\sigma}}_{n+1}^{(i)} - \bar{\boldsymbol{\sigma}}_{n+1}; \qquad \bar{\boldsymbol{\sigma}}_{n+1}^{vp} = \bar{\boldsymbol{\sigma}}_{n+1}^{vp(i)} + \Delta\bar{\boldsymbol{\sigma}}_{n+1}^{vp}; \text{EXIT.}$$

should play a dominant role in the material modeling. By contrast, the accuracy and convergence properties of the proposed algorithmic treatment, based on the notion of operator splitting, can be precisely evaluated. For the elastoplastic cap model without a damage mechanism, the accuracy of the return mapping part employing a closest-point-projection has been characterized in Ref. [3] by means of iso-error maps. In this paper, however, the return mapping is based on a cutting-plane procedure proposed in Ref. [4] and, in addition, the operator split is generalized to include the damage mechanism. Since the accuracy analysis of return mappings employing the cutting-plane algorithm is contained in Ref. [2], the emphasis in this section is placed on to the convergence properties of the new algorithm extended to include damage mechanisms. In all the numerical simulations that follow use will be made of the inviscid ductile cap-damage model for concrete summarized in Section 6.1 of Part I.

4.3.1. *Uniaxial compression tests*[16]. In this first example we consider uniaxial compression tests reported in Ref. [16] for three unconfined concrete specimens with the following values of the characteristic strength f_c': (a) 10.7 ksi, (b) 7.3 ksi, and (c) 5.8 ksi. The initial (undamaged) bulk and shear moduli for the three specimens are independently determined to be 2222.222 and 1666.667 ksi for (a), 1722.222 and 1291.667 ksi for (b), and 1388.889 and 1041.667 ksi for (c). Optimal values for the parameters in the cap-damage model of Section 6.1 of Part I are obtained by means of least square fit employing the Marquardt–Levenberg algorithm, as described in Refs [3, 17]. The normalized relative r.m.s. errors of the fittings are found to be $\delta = 1.85\%$ for test (a), $\delta = 1.33\%$ for test (b), and $\delta = 1.87\%$ for test (c). Both the experimental data and the numerical results are shown in Figs 2–4. From these figures we note the remarkably good *qualitative* and *quantitative* agreement between the model and the experimental results. In particular, we observe that the strain-softening effect due to damage is fully captured by the model.

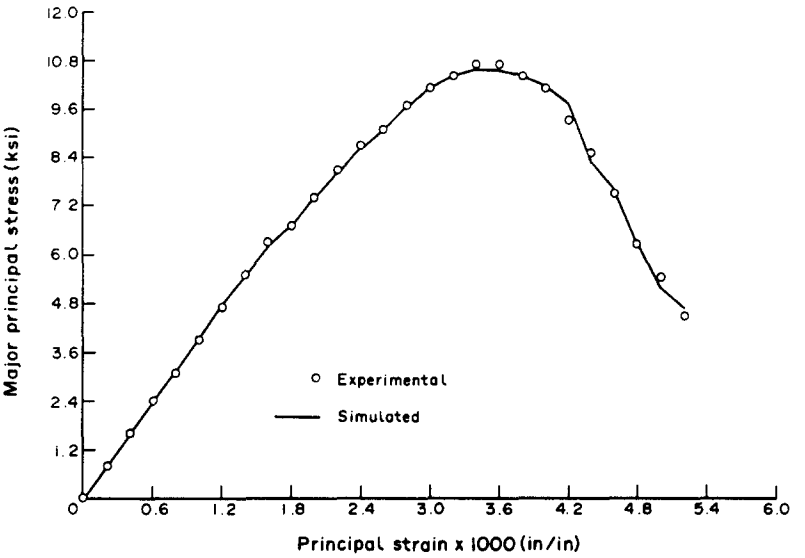

Fig. 2. Comparison of the experimental and simulated stress–strain curve for uniaxial compression test of $f'_c = 10.7$ ksi concrete specimen[16]. This test was performed under strain control. The initial bulk and shear moduli are determined as 2222.222 and 1666.667 ksi, respectively. The vertical axis is the major principal stress (σ_{33}) and the horizontal axis denotes the major principal strain (ε_{33}). The circle symbols and the solid line represent the experimental and the simulated response, respectively. The normalized relative r.m.s. error measure of the simulated response (with respect to the experimental data) δ is 1.85%.

4.3.2. *Colorado concrete data*[3, 9]. The data for this example are taken from the well-documented experimental program conducted at the University of Colorado[9] on a systematic three-dimensional testing of concrete. The program consists of six major series of non-conventional multiaxial cyclic stress–strain curves. It is noted that replicate tests were run for some experiments, which enable us to assess the relative consistency of experimental data. A data consistency analysis procedure is employed which generally indicates reasonable consistency of the data measurements, although some serious discrepancies are also observed. It should be emphasized that one cannot, in general, expect the

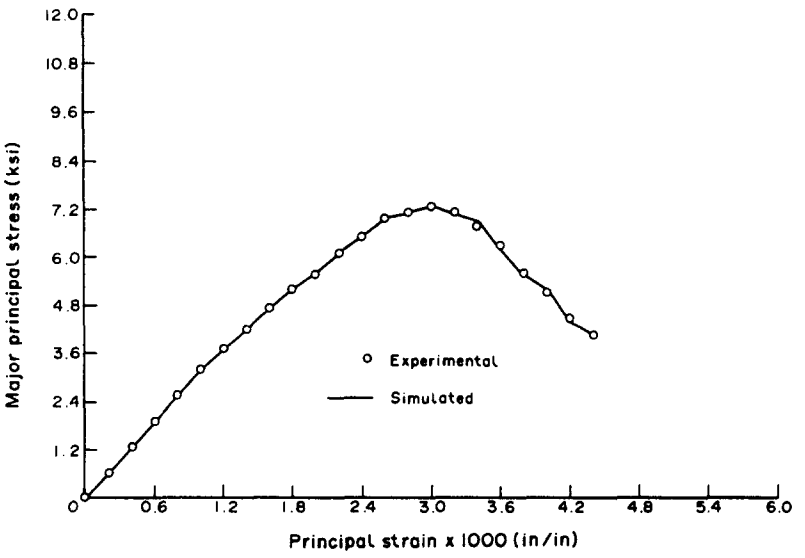

Fig. 3. Comparison of the experimental and simulated stress–strain curve for uniaxial compression test of $f'_c = 7.3$ ksi concrete specimen. The initial bulk and shear moduli are determined as 1722.222 and 1291.667 ksi, respectively. The normalized relative r.m.s. error measure of the simulated response δ is 1.33%.

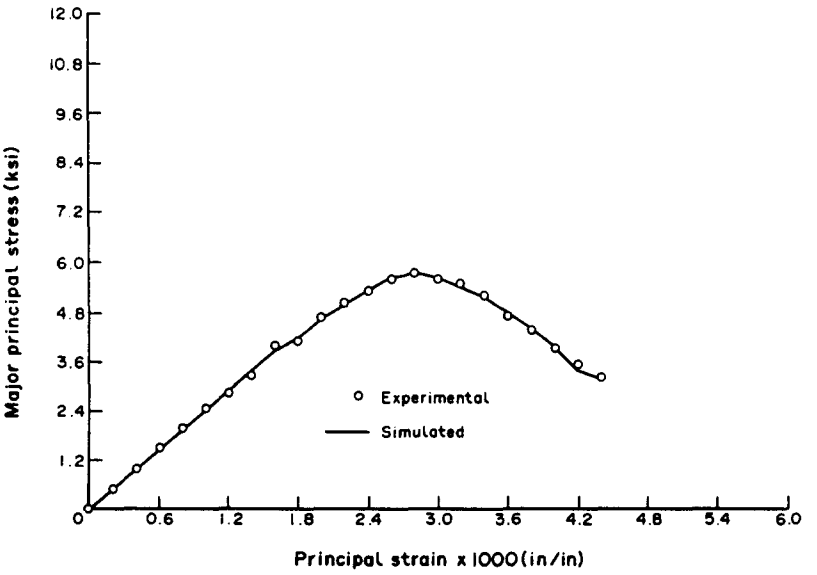

Fig. 4. Comparison of the experimental and simulated stress–strain curve for uniaxial compression test of f'_c = 5.8 ksi concrete specimen. The initial bulk and shear moduli are determined as 1388.889 and 1041.667 ksi, respectively. The normalized relative r.m.s. error measure of the simulated response δ is 1.87%.

performance of the numerical simulation to be better than the associated data consistency measure. The numerical results reported below not only include fitting of the model to complicated stress paths but, in addition, *predictions* of material behavior obtained by exercising the model against experimental results. This is possible due to the existence of experimental results intended to replicate the same loading path.

Circular stress path tests (I). Tests 3-3, 3-4, 3-8, and 3-9 are replicates concerning the following loading paths. The specimens are first subjected to hydrostatic monotonic loading to a specified deviatoric plane, followed by deviatoric loading along the triaxial compression path until completion of the specified circular path. The model parameters are obtained by optimal fitting with respect to test 3-3, using the least square procedure described in Refs [3, 17]. These parameters are then employed in the subsequent simulations intended to predict the behavior observed in other replicates of this test—tests 3-4, 3-8, and 3-9—under significant experimental data perturbations (ranging from 7 to 47%). The normalized relative r.m.s. error δ for the fitting (test 3-3) is δ = 5.97%, whereas the normalized relative r.m.s. error found in the prediction of the replicates is δ = 17.1% for test 3-4, δ = 24.4% for test 3-8, and δ = 11.96% for test 3-9. In spite of considerable data corruption, good overall predictive capability of the model is observed, as illustrated in Figs 5–8.

Circular stress path tests (II). Tests 3-5 and 3-6 are also concerned with circular stress paths, but here on octahedral planes different from those in the preceding set. Test 3-5 is taken as a fitting reference; an optimal least square fit produces a normalized relative r.m.s. error of δ = 5.36%. The prediction is made with respect to test 3-6 (replicate), leading to a normalized relative r.m.s. error of δ = 8.44%. Note that the data corruption percentage (dimensionless data consistency index) is 7.5%, which is considered to be good. The results are shown in Figs 9 and 10. Both the qualitative and quantitative agreement found with the experimental results are excellent.

Axisymmetric triaxial compression tests. Tests 4-1 and 4-2 are intended to explore concrete response subject to axisymmetric stress histories. The optimal fitting for test 4-1 yields δ = 9.27% and the prediction for test 4-2 (replicate) gives δ = 12.48%. The dimensionless data consistency index for this case is 10.9%. The results are shown in Figs 11 and 12. The qualitative agreement in the prediction is satisfactory although a softer response is found relative to the experimental results.

Cyclic triaxial extension tests. This simulation is concerned with tests 1-3 and 1-12 which are intended to assess the response of concrete to triaxial loading cycles. Again two replicates

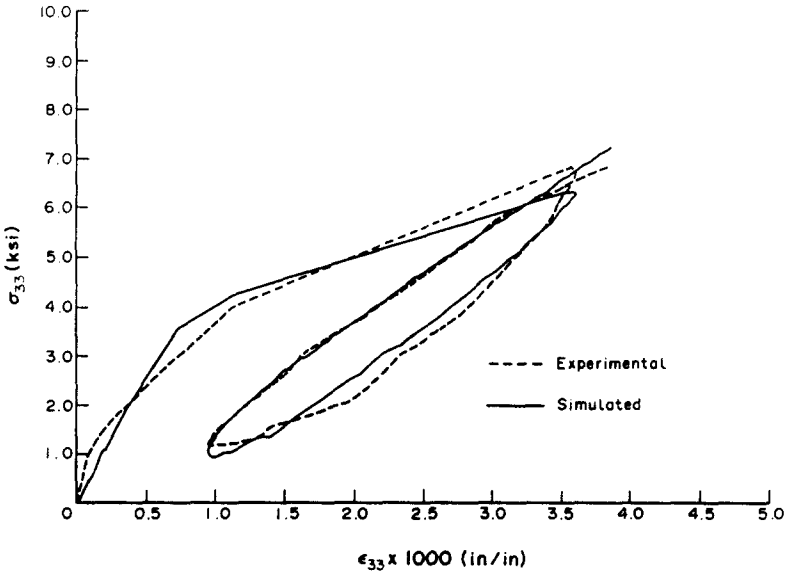

Fig. 5. Comparison of the experimental and simulated (*fitted*) data for Colorado concrete test 3-3. This is a circular stress path on the 12 ksi octahedral plane. The vertical axis is the σ_{33} stress and the horizontal axis is the ε_{33} strain. The dashed and solid lines represent the experimental and the simulated (*fitted*) response, respectively. The normalized relative r.m.s. error measure of the simulated (*fitted*) response δ is 5.97%.

are considered to illustrate the fitting and predictive abilities of the model. The data consistency index is found to be 26% (not very good). An optimal fit relative to test 1-3 is performed leading to a normalized relative r.m.s. error of $\delta = 3.8\%$. The prediction of test 1-12 then yields a normalized relative r.m.s. error of $\delta = 15.76\%$. Once more good qualitative agreement is found between experimental and numerical results, as shown in Figs 13 and 14.

Cyclic simple shear tests. Tests 2-3 and 2-4 are intended to explore concrete response to deviatoric simple shear cycles with stress reversal about the hydrostatic state. The data consistency index for the two tests is 9.7%, which is considered to be good. The optimal

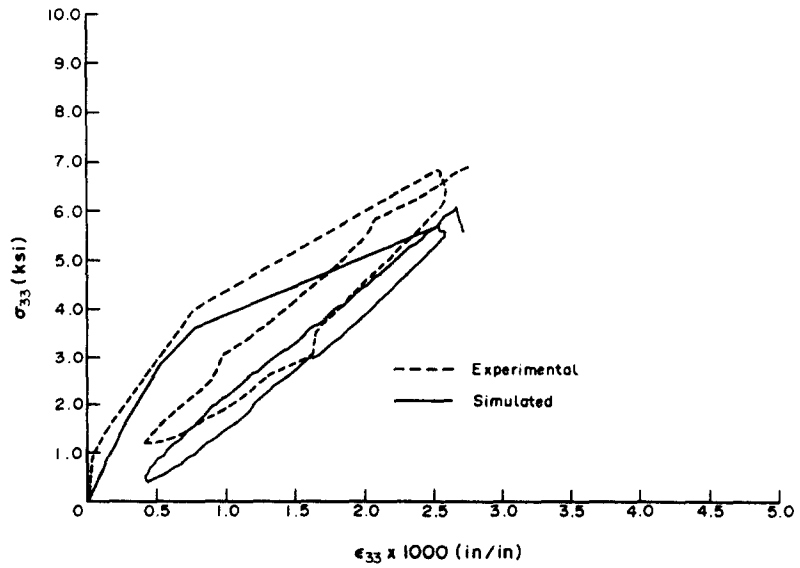

Fig. 6. Comparison of the experimental and simulated (*predicted*) data for Colorado concrete test 3-4. This is a replicate of test 3-3. It is noted that the prediction curve is based on the model parameters obtained by fitting test 3-3. The normalized relative r.m.s. error measure of the *predicted* response δ is 17.1%.

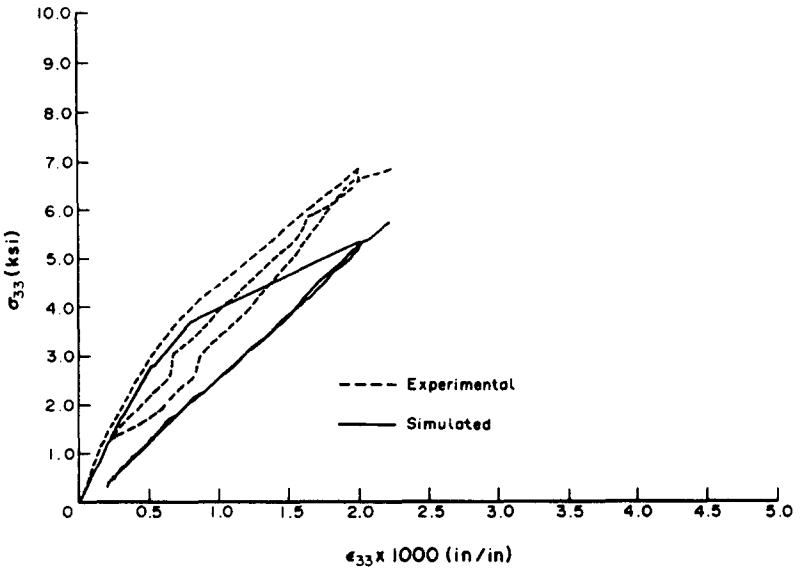

Fig. 7. Comparison of the experimental and simulated (*predicted*) data for Colorado concrete test 3-8. This is also a replicate of test 3-3. It is noted that the prediction curve is based on the model parameters obtained by fitting test 3-3. The normalized relative r.m.s. error measure of the *predicted* response δ is 24.48%.

fitting for test 2-4 yields $\delta = 7.7\%$ and the prediction for test 2-3 (replicate) gives $\delta = 10.33\%$. The results are shown in Figs 15 and 16. The overall qualitative agreement in the prediction is satisfactory.

Remark 4.3 (*Alternative characterization*). It is interesting to compare the above results with numerical simulations obtained with the alternative formulation based on Remark 3.7 of Part I. Figure 17 shows the numerical simulation obtained by exercising this model with parameters *fitted* to the circular stress path test 3-3 of the Colorado concrete data. Figures 18–20 show the corresponding results *predicted* by this alternative model for the replicate tests 3-4, 3-8 and 3-9. Similar comparisons were made for the remaining Colorado concrete

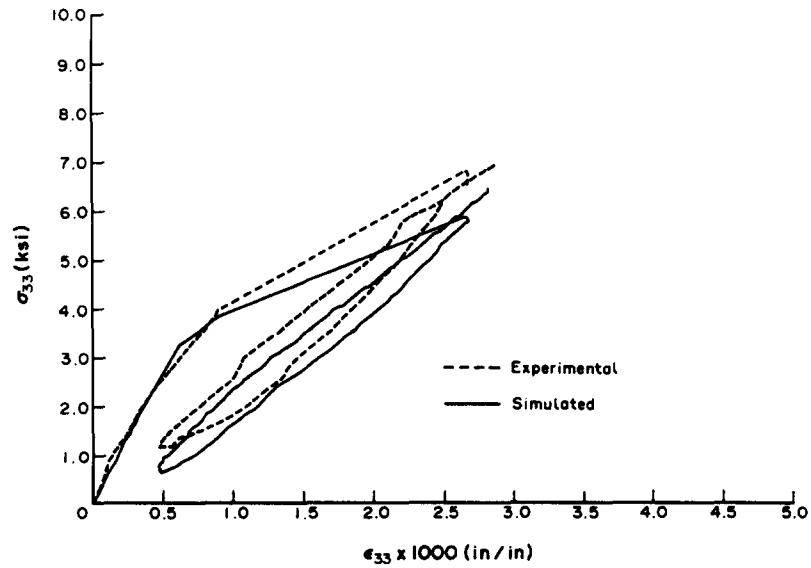

Fig. 8. Comparison of the experimental and simulated (*predicted*) data for Colorado concrete test 3-9. This is another replicate of test 3-3. It is noted that the prediction curve is based on the model parameters obtained by fitting test 3-3. The normalized relative r.m.s. error measure of the *predicted* response δ is 11.96%.

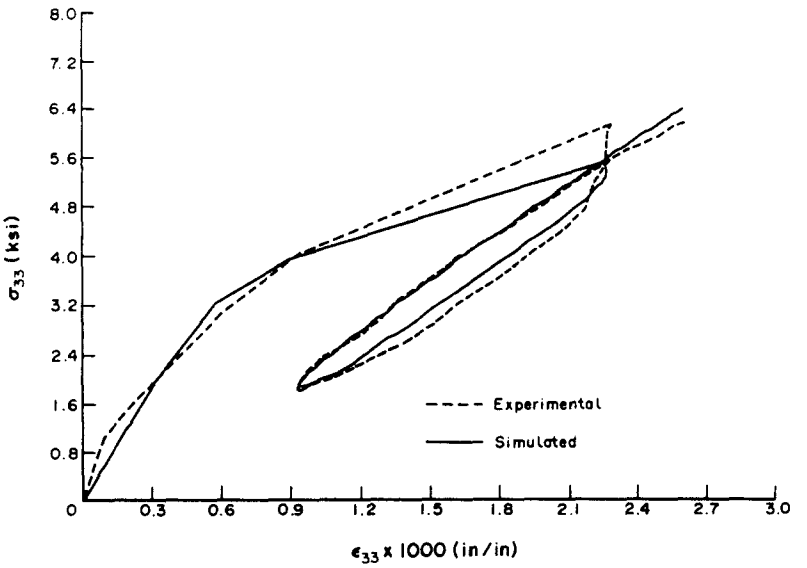

Fig. 9. Comparison of the experimental and simulated (*fitted*) data for Colorado concrete test 3-5. This is also a circular stress path on the 12 ksi octahedral plane. The normalized relative r.m.s. error measure of the simulated (*fitted*) response δ is 5.36%.

tests considered in Section 4.3.2. We conclude that, in general, the numerical results obtained by using eqns (26) in Part I are satisfactory. It is noted, however, that the plastic characterization based on eqns (19) of Part I consistently provides better fitting results than the characterization based on eqns (26) of Part I. □

4.3.3. *Convergence characteristics of the algorithm.* We recall that within the proposed operator split, damage is taken into account in the (elastic-damage) predictor phase where the elastic-damage moduli are computed. In the plastic corrector phase, the elastic-damage moduli remain unchanged and the return path is approximated by sequence of segments that return the stress point to the updated yield surface at a *quadratic* rate of convergence.

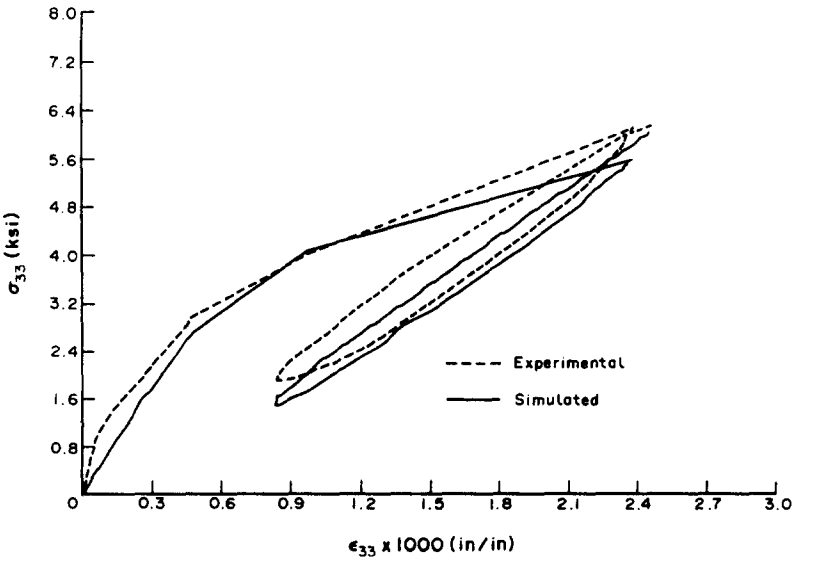

Fig. 10. Comparison of the experimental and simulated (*predicted*) data for Colorado concrete test 3-6. This is a replicate of test 3-5. It is noted that the prediction curve is based on the model parameters obtained by fitting test 3-5. The normalized relative r.m.s. error measure of the *predicted* response δ is 8.44%.

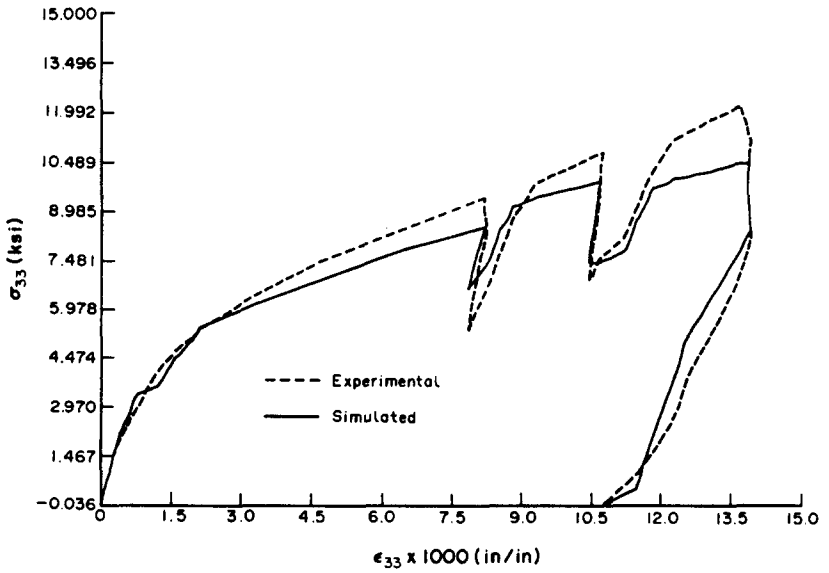

Fig. 11. Comparison of the experimental and simulated (*fitted*) data for Colorado concrete test 4-1. This is a cyclic axisymmetric triaxial compression test. The normalized relative r.m.s. error measure of the simulated (*fitted*) response δ is 9.27%.

Since the elastic-damage predictor reduces to a mere function evaluation, an assessment of the efficiency of the overall algorithm is provided by the number of iterations to convergence of the cutting plane return mapping algorithm. In addition, the Euclidean norm of the constitutive residual, measuring the distance of the stress point to the yield surface at each loading step, must exhibit a quadratic rate of asymptotic convergence.

Both the number of iterations to convergence and the rate of convergence to zero of the constitutive residual are numerically illustrated in the simulation corresponding to Test 3-5 of the Colorado concrete data. Representative iteration counts are summarized in Table 1, and numerical values of the Euclidean norm of the constitutive residual for typical iterations are displayed in Table 2. The good overall performance of the numerical

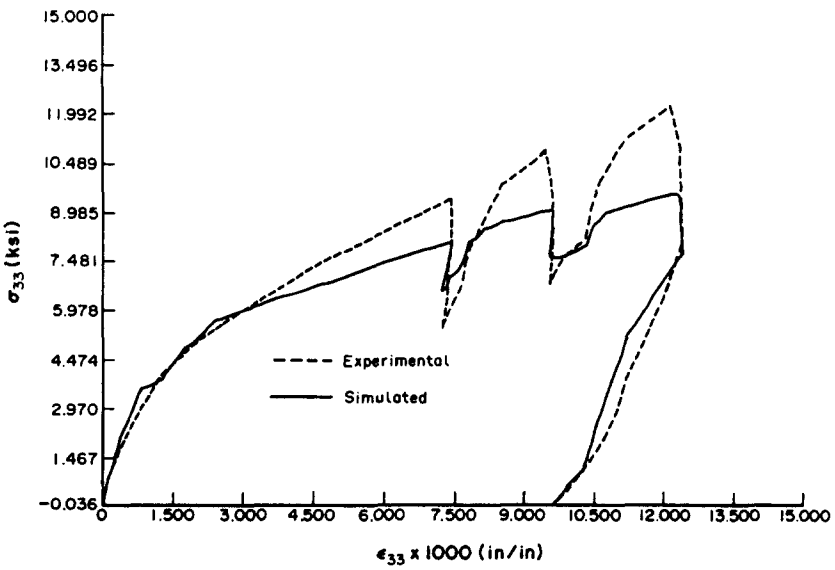

Fig. 12. Comparison of the experimental and simulated (*predicted*) data for Colorado concrete test 4-2. This is a replicate of test 4-1. It is noted that the prediction curve is based on the model parameters obtained by fitting test 4-1. The normalized relative r.m.s. error measure of the *predicted* response δ is 12.48%.

Table 1. Number of iterations for each loading step in test 3-5

Step	5	6	8	9	10	11	12	13	14	15
Count	3	4	3	3	3	3	3	3	3	3

Table 2. Residual values for typical loading steps in test 3-5

Iteration	0	1	2	3	4
Step 5	0.291e+1	0.131e+0	0.414e−3	0.418e−8	—
Step 6	0.172e+2	0.271e+1	0.133e+1	0.389e−3	0.338e−8
Step 8	0.246e+0	0.131e−2	0.378e−7	0.223e−15	—
Step 9	0.499e+0	0.524e−2	0.603e−6	0.822e−14	—
Step 10	0.109e+1	0.237e−1	0.123e−4	0.332e−11	—

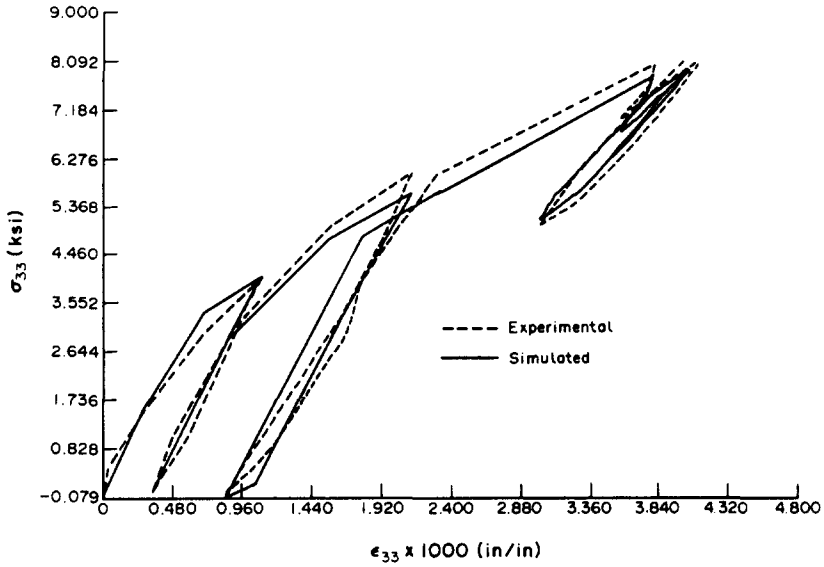

Fig. 13. Comparison of the experimental and simulated (*fitted*) data for Colorado concrete test 1-3. This is a cyclic triaxial extension test. The normalized relative r.m.s. error measure of the simulated (*fitted*) response δ is 3.8%.

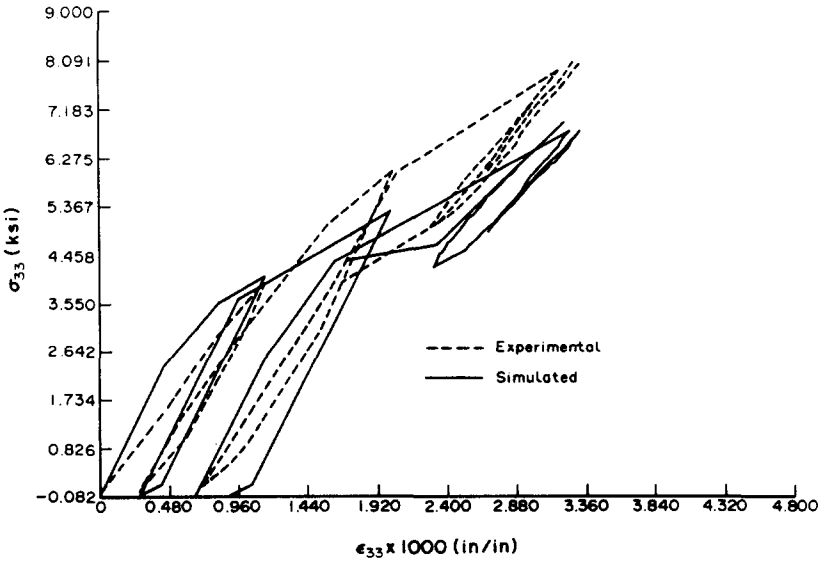

Fig. 14. Comparison of the experimental and simulated (*predicted*) data for Colorado concrete test 1-12. This is a cyclic triaxial extension test. It is noted that the prediction curve is based on the model parameters obtained by fitting test 1-3. The normalized relative r.m.s. error measure of the *predicted* response δ is 15.76%.

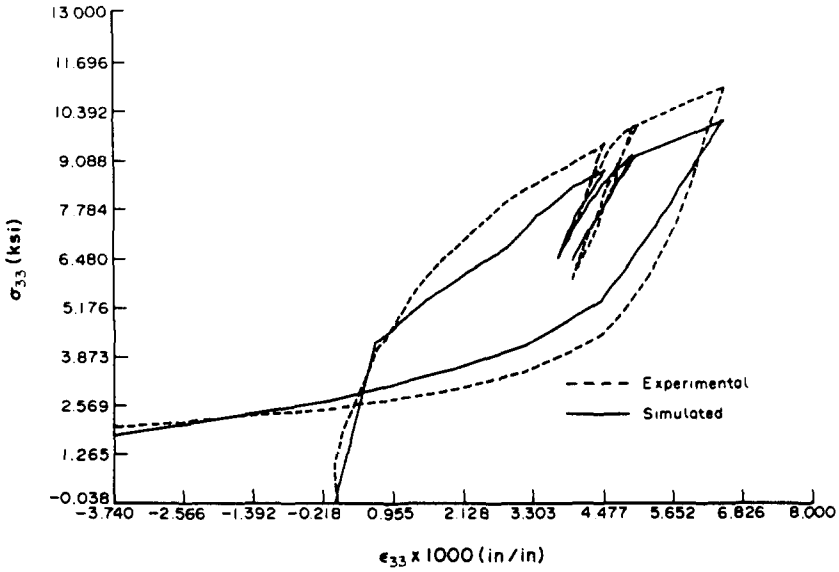

Fig. 15. Comparison of the experimental and simulated (*fitted*) data for Colorado concrete test 2-4. This is a simple shear path in 8 ksi deviatoric plane with cyclic stress reversal. The normalized relative r.m.s. error measure of the simulated (*fitted*) response δ is 7.7%.

algorithm is apparent from these results, and the *quadratic rate of asymptotic convergence* is clearly demonstrated.

It is emphasized that the structure of the return mapping algorithm is exactly the same for both ductile and brittle damage cases. Hence, aside from the additional eigenvalue calculation, the numerical performance of the algorithm in both cases is identical.

4.4. *Numerical examples: rate-dependent case*

We present below simulations performed with the visco-damage algorithm in Box 1A on the basis of two sets of recent dynamic concrete tests[18–20].

4.4.1. *Uniaxial compression tests*[19, 20]. As a first example we consider uniaxial compression tests reported in Refs [19, 20] for concrete specimens under two different

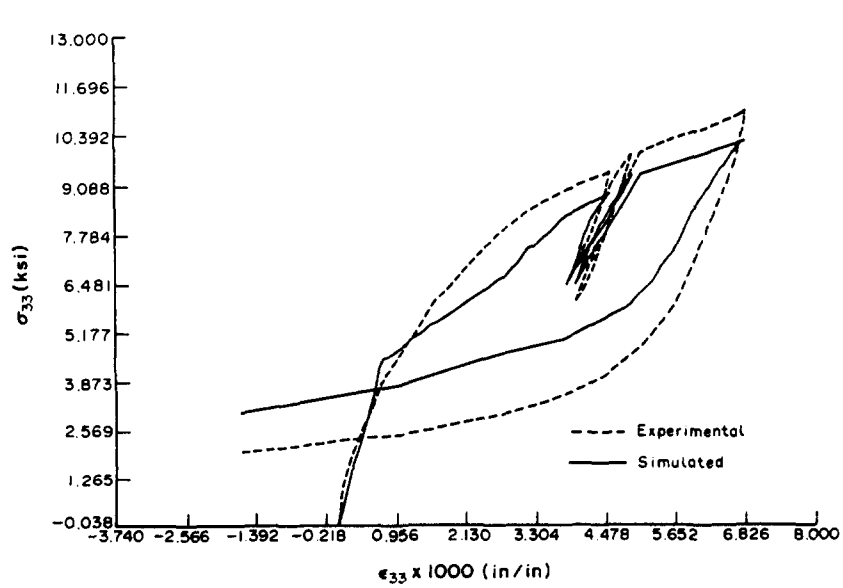

Fig. 16. Comparison of the experimental and simulated (*predicted*) data for Colorado concrete test 2-3. This is a replicate of test 2-4. It is noted that the prediction curve is based on the model parameters obtained by fitting test 2-4. The normalized relative r.m.s. error measure of the *predicted* response δ is 10.33%.

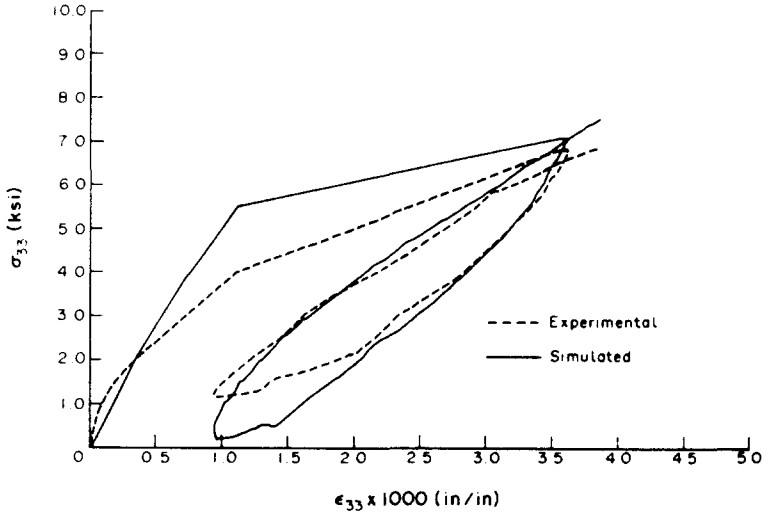

Fig. 17. Comparison of the experimental and simulated (*fitted*) data for Colorado concrete test 3-3. This is a circular stress path on the 12 ksi octahedral plane. The vertical axis is the σ_{33} stress and the horizontal axis is the ε_{33} strain. The dashed and solid lines represent the experimental and the simulated (*fitted*) response, respectively. The normalized relative r.m.s. error measure of the simulated (*fitted*) response δ is 11.7%.

constant strain rates. The initial values of the undamaged elastic moduli and Poisson ratio are: $E = 6000$ ksi and $\nu = 0.22$ for the concrete specimens used. The (static) uniaxial compressive strength is estimated to be 6.79 ksi. Two different visco-damage models are employed to simulate numerically the material response for fast loading ($\dot{\varepsilon} = 0.088\ s^{-1}$) and slow loading ($\dot{\varepsilon} = 1.0e-6\ s^{-1}$).

Elasto-viscoplastic-visco-damage model. The first simulation is obtained by using the model outlined in Section 6.2, including viscous damage, as outlined in Section 3.4 of Part I. Figure 21 shows the experimental and numerical results at two strain rates. We note the good *qualitative* and *quantitative* agreement between the model and the experimental data. The rate enhancement of stress response due to the viscous mechanism is clearly demonstrated. In particular, we observe that the strain-softening effect due to damage is fully captured.

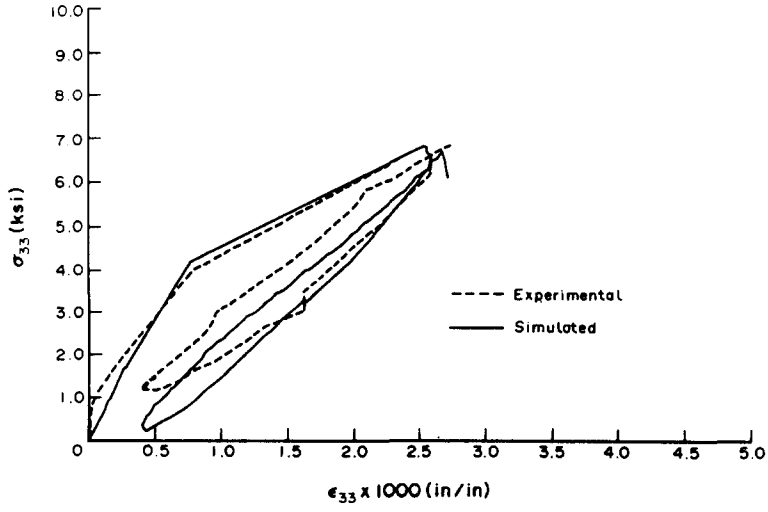

Fig. 18. Comparison of the experimental and simulated (*predicted*) data for Colorado concrete test 3-4. This is a replicate of test 3-3. It is noted that the prediction curve is based on the model parameters obtained by fitting test 3-3. The normalized relative r.m.s. error measure of the *predicted* response δ is 11.7%.

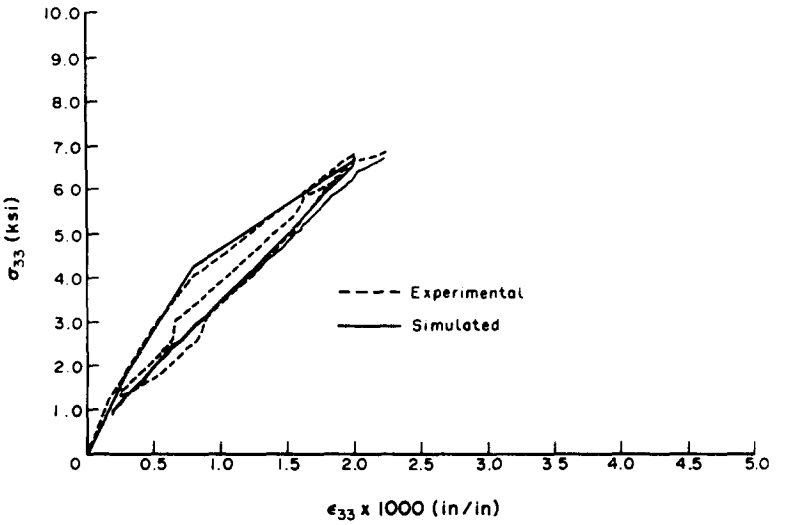

Fig. 19. Comparison of the experimental and simulated (*predicted*) data for Colorado concrete test 3-8. This is also a replicate of test 3-3. It is noted that the prediction curve is based on the model parameters obtained by fitting test 3-3. The normalized relative r.m.s. error measure of the *predicted* response δ is 5.95%.

Elastic-visco-damage model. Two features are apparent from the two uniaxial compression tests in Fig. 21. First, no local unloading takes place, and second, the level of strains is low. This suggests neglecting plastic flow, and motivates the use of the much simpler elastic-visco-damage model to predict the material response. The results are shown in Fig. 22. Reasonably good agreement between simulation and experimental results is obtained by using the elasto-visco-damage model. Nevertheless, one would expect loss of accuracy of this simple model as the level of strains increases and plastic deformation becomes significant.

From the above simulations, we observe a decrease in the degree of non-linearity of the stress–strain curve as the strain rate increases. Furthermore, the value of d measuring the amount of microcracking at a particular strain level decreases as the constant strain rate increases. In other words, growth of micro-cracks is *retarded* at higher strain rates. This is in agreement with the experimental results reported in Refs [19, 21, 22].

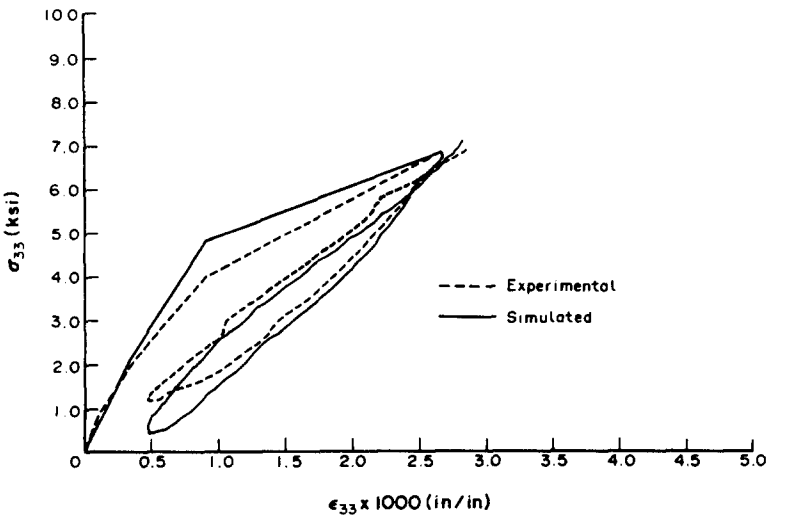

Fig. 20. Comparison of the experimental and simulated (*predicted*) data for Colorado concrete test 3-9. This is another replicate of test 3-3. It is noted that the prediction curve is based on the model parameters obtained by fitting test 3-3. The normalized relative r.m.s. error measure of the *predicted* response δ is 8.17%.

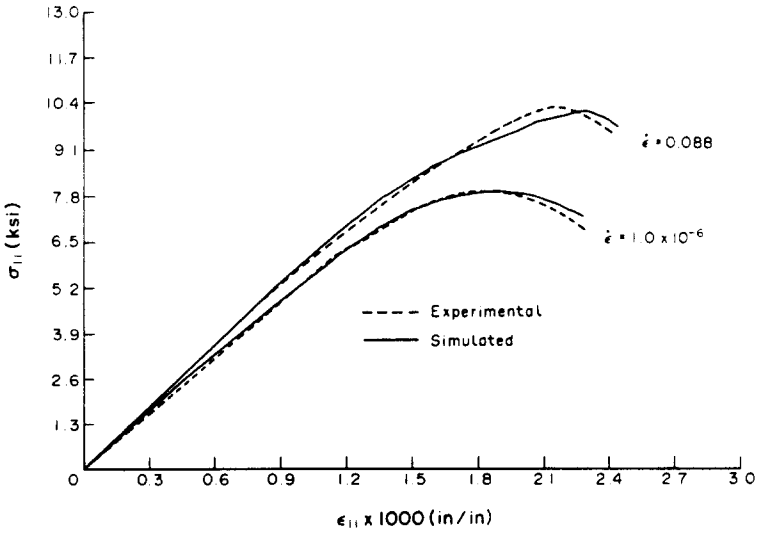

Fig. 21. Comparison of the experimental and simulated dynamic stress–strain curves for uniaxial compression test of concrete specimens. The specimens are under two different constant strain rates. The elasto-viscoplastic-visco-damage model is employed in this numerical simulation.

4.4.2. *TerraTek Research dynamic concrete test No.* 33[18]. This test is concerned with a concrete specimen composed of limestone, coarse aggregate and other ingredients. The initial hydrostatic pressure is 5 ksi, but the initial axial and transverse strains (corresponding to the initial pressure) are essentially zero. This indicates the pre-existence of significant plastic strains (or plastic relaxation stresses) in the initial conditions and hence precludes the use of a simple elastic-visco-damage model. It is also noted that the strain rate is variable throughout the test. Figure 23 shows the experimental data as well as the simulated results. Reasonably good qualitative reproduction of the main features for this dynamic test is observed.

5. CLOSURE

A basic purpose of the present work has been to demonstrate that the proposed classes of elastoplastic-damage constitutive equations are particularly well suited for large-scale

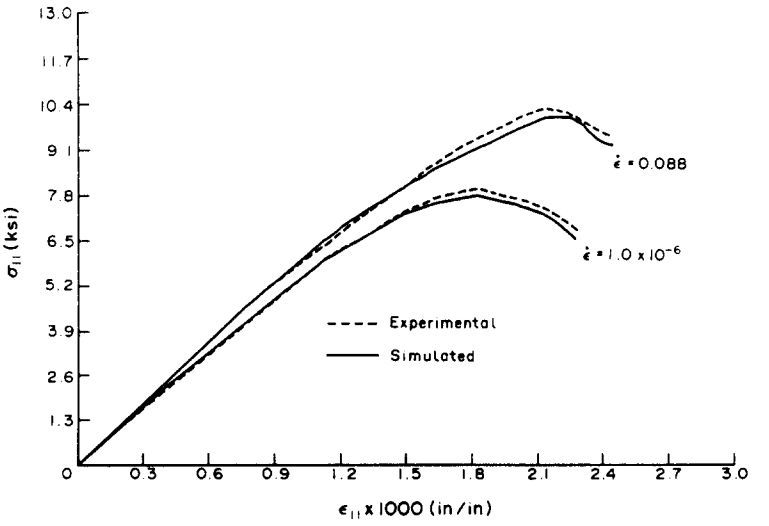

Fig. 22. Comparison of the experimental and simulated dynamic stress–strain curves for uniaxial compression test of concrete specimens. The elasto-visco-damage model is employed in this numerical simulation.

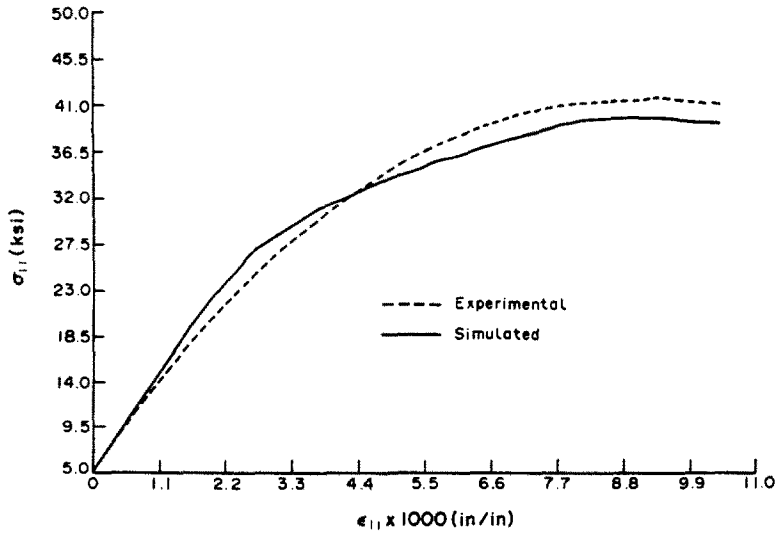

Fig. 23. Comparison of the experimental and simulated stress–strain curves for TerraTek Research dynamic concrete test No. 33. The elasto-viscoplastic-visco-damage model is employed in this numerical simulation.

computation. To this end, we have outlined a new variational framework for the numerical implementation of elastoplastic-damage models. By making systematic use of the operator splitting methodology, we have developed a general class of integration algorithms which, in addition to isotropic and anisotropic damage, are capable of accommodating general elastic–plastic response. Both cases of strain- and stress-based damage mechanisms have been considered. For the latter, we have proposed a new three-step operator split. As a specific example, we have specialized the class of algorithms based on a strain space formulation to the cap-damage model for concrete. Moreover, the algorithmic implementation of this model has been examined in detail, in particular, the proper algorithmic treatment of the singular (corner) point on the yield surface. Finally we have extended the proposed algorithmic treatment to accommodate viscoplastic rate-dependent effects.

It is emphasized that, from a computational standpoint, the implementation the proposed ductile and brittle *anisotropic* strain-based damage models requires only a trivial modification in the elastic predictor phase of existing return mapping algorithms for rate-independent and rate-dependent plasticity.

A number of numerical simulations have been presented that illustrate the good qualitative agreement between well-documented experimental data for concrete and the simple cap-damage model. In particular, softening behavior is remarkably well captured. These simulations also demonstrate the good performance of the proposed algorithm.

The qualitative agreement found between experimental results and simulations performed with the visco-damage model is encouraging. Although of a preliminary nature, these simulations suggest that a viscous regularization of rate-independent damage models of the type discussed may be suitable for modeling rate-sensitive damage behavior in concrete materials.

Acknowledgements—We are indebted to Profs K. S. Pister and R. L. Taylor for many helpful discussions. This work was sponsored by the Defense Nuclear Agency under Contract No. DNA-2DJA739 with Stanford University, and Contract No. DNA001-84-C-0304 with the University of California, Berkeley. This support and the interest and comments of Dr Eugene Sevin are gratefully acknowledged.

REFERENCES

1. R. D. Krieg and D. B. Krieg, Accuracies of numerical solution methods for the elastic–perfectly plastic model. *ASME J. Pressure Vessel Tech.* **99**, 510–515 (1977).
2. M. Ortiz and J. C. Simo, An analysis of a new class of integration algorithms for elastoplastic constitutive relations. *Int. J. Numer. Meth. Engng* (1987), in press.
3. J. C. Simo, J. W. Ju, K. S. Pister and R. L. Taylor, An assessment of the cap model: consistent return

algorithms and rate-dependent extension. Report No. UCB/SESM-85/05, Department of Civil Engineering, University of California, Berkeley (May 1985).
4. J. C. Simo and M. Ortiz, A unified approach to finite deformation elastoplasticity based on the use of hyperelastic relations. *Comp. Meth. Appl. Mech. Engng* **49**, 221–245 (1985).
5. J. C. Simo and R. L. Taylor, Consistent tangent operators for rate independent elastoplasticity. *Comp. Meth. Appl. Mech. Engng* **48**, 101–118 (1984).
6. J. C. Simo and R. L. Taylor, A return mapping algorithm for plane stress elastoplasticity. *Int. J. Numer. Meth. Engng* (1987), in press.
7. J. C. Simo, R. L. Taylor and K. S. Pister, Variational and projection methods for the volume constraint in finite deformation elastoplasticity. *Comp. Meth. Appl. Mech. Engng* **51**, 177–188 (1985).
8. M. L. Wilkins, Calculation of elastic–plastic flow. In *Methods of Computational Physics* (Edited by B. Alder *et al.*), Vol. 3. Academic Press, New York (1964).
9. R. Scavuzzo, T. Stankowski, K. H. Gerstle and H. Y. Ko, Stress–strain curves for concrete under multiaxial load histories. NSF CME-80-01508, Department of Civil Engineering, University of Colorado, Boulder (August 1983).
10. J. C. Simo and T. J. R. Hughes, On the variational foundations of assumed strain methods. *J. Appl. Mech.* (1987), in press.
11. J. E. Marsden and T. J. R. Hughes, *Mathematical Foundations of Elasticity*. Prentice-Hall, Englewood Cliffs, New Jersey (1983).
12. M. Gurtin, *An Introduction to Continuum Mechanics*. Academic Press, New York (1981).
13. A. Chorin, T. J. R. Hughes, M. F. McCracken and J. E. Marsden, Product formulas and numerical algorithms. *Commun. Pure Appl. Math.* **31**, 205–256 (1978).
14. D. G. Luenberger, *Introduction to Linear and Nonlinear Programming*, 2nd Edn. Addison-Wesley, Reading, Massachusetts (1984).
15. I. S. Sandler and D. Rubin, An algorithm and a modular subroutine for the cap model. *Int. J. Numer. Analyt. Meth. Geomech.* **3**, 173–186 (1979).
16. P. T. Wang, Complete stress–strain curve of concrete and its effect on ductility of reinforced concrete members. Ph.D. Thesis, University of Illinois at Chicago Circle (October 1977).
17. J. W. Ju, J. C. Simo, K. S. Pister and R. L. Taylor, A parameter estimation algorithm and extensive numerical simulation for the cap model. Report No. UCB/SESM-85/10, Department of Civil Engineering, University of California, Berkeley (November 1985).
18. K. Bakhtar *et al.*, Concrete material properties. TerraTek Research, DNA Concrete Meeting, Utah (April 1985).
19. W. Suaris and S. P. Shah, Rate-sensitive damage theory for brittle solids. *J. Engng Mech. ASCE* **110**(6), 985–997 (June 1984).
20. W. Suaris, Dynamic behavior of concrete: a phenomenological theory and instrumented impact testing. Ph.D. Thesis, Northwestern University, Evanston, Illinois (1983).
21. J. Takeda and H. Tachikawa, Deformation and fracture of concrete subjected to dynamic load. *Proc. Int. Conf. on Mech. Behavior of Mater.*, Vol. 4, *Concrete and Cement Paste Glass and Ceramics*, Kyoto, 15–20 Aug., pp. 267–277 (1971).
22. W. Suaris and S. P. Shah, Properties of concrete subjected to impact. *J. Struct. Engng ASCE* **109**(ST7), 1727–1741 (July 1983).
23. J. C. Simo and T. Honein, Variational formulation, discrete conservation laws and path-domain independent integrals for elasto-visco-plasticity. *J. Appl. Mech.* (submitted).

APPENDIX: RETURN MAPPING ALGORITHM FOR CAP MODEL

We shall derive the cutting plane algorithm for the strain-based damage model featuring stress split. Consider the linearization of the consistency condition ($f = 0$) about current values of the state variables. We have

$$f^{(i)}_{n+1} = \Delta\lambda^{(i+1)}_{n+1}\left[\frac{\partial f}{\partial \bar{\boldsymbol{\sigma}}} : \mathbf{C}^0 : \frac{\partial f}{\partial \bar{\boldsymbol{\sigma}}}\right]^{(i)}_{n+1} - \left.\frac{\partial f}{\partial \kappa}\right|^{(i)}_{n+1} \Delta\kappa^{(i+1)}_{n+1} \tag{A1}$$

where use has been made of the fact that during the plastic corrector phase, $\Delta\bar{\boldsymbol{\sigma}} = -\Delta\bar{\boldsymbol{\sigma}}^{\mathrm{p}} = -\Delta\lambda\mathbf{C}^0 : \partial f/\partial\bar{\boldsymbol{\sigma}}$. Let us now introduce the following notation with reference to eqns (74) in Part I:

$$\bar{\Omega} := \begin{cases} 2F_{\mathrm{c}}(\bar{J}_1)F'_{\mathrm{c}}(\bar{J}_1) & \text{(failure envelope)} \\ -\dfrac{2}{R^2}(\bar{J}_1 - L(\kappa)) & \text{(cap surface)} \end{cases} \tag{A2}$$

where a prime denotes differentiation with respect to the argument. From eqn (73) of Part I and eqn (A2), we obtain

$$\left.\frac{\partial f}{\partial \bar{\boldsymbol{\sigma}}}\right|^{(i)}_{n+1} = [\bar{\mathbf{s}} - \bar{\Omega}\,\mathbf{1}]^{(i)}_{n+1} \tag{A3}$$

where $\bar{\mathbf{s}}$ denotes the effective stress deviator. From Remark 3.2 of Part I it follows that the plastic strain rate is given by

$$\dot{\boldsymbol{\varepsilon}}^{\mathrm{p}} := \left[\left.\frac{\partial^2 \Psi^0}{\partial \boldsymbol{\varepsilon}^2}\right|_{\boldsymbol{\varepsilon}^{\mathrm{p}}}\right]^{-1} : \dot{\bar{\boldsymbol{\sigma}}}^{\mathrm{p}}$$

where $\dot{\bar{\sigma}}^p$ is the effective plastic stress rate. Hence, from eqn (A3) we obtain

$$\Delta\varepsilon_v^p \equiv \operatorname{tr}\Delta\boldsymbol{\varepsilon}^p \equiv \Delta\lambda \operatorname{tr}\frac{\partial f}{\partial\boldsymbol{\sigma}} = -3\Delta\lambda\bar{\Omega}. \tag{A4}$$

On the other hand, linearization of the plastic hardening law yields $\Delta\varepsilon_v^p = (\mathrm{d}h(\kappa)/\mathrm{d}\kappa)\,\Delta\kappa$. This result along with eqn (A4) leads to

$$\Delta\lambda_{n+1}^{(i+1)} = -\frac{h'(\kappa)}{3\bar{\Omega}}\Delta\kappa_{n+1}^{(i+1)} \tag{A5}$$

where $h'(\kappa) := (\mathrm{d}h(\kappa)/\mathrm{d}\kappa)$. Substitution of eqn (A5) into eqn (A1) then gives the final expression recorded in Box 2.2, i.e.

$$\Delta\kappa_{n+1}^{(i+1)} = \left.\frac{f}{-\dfrac{\partial f}{\partial\kappa} - \dfrac{\dfrac{\partial f}{\partial\bar{\sigma}} : \mathbf{C}^0 : \dfrac{\partial f}{\partial\bar{\sigma}}h'(\kappa)}{3\bar{\Omega}}}\right|_{n+1}^{(i)}. \tag{A6}$$

For the *singular corner mode*, a separate derivation is required. We start by noting that in the corner mode the constraint $\kappa_{n+1} = J_{1_{n+1}}$ must hold. By enforcing this constraint we can compute a scaling factor η such that $\kappa_{n+1} = J_{1_{n+1}}$ is satisfied. After some algebra, the value of η is found to be

$$\eta = [J_{n+1}^{(i)} - \kappa_{n+1}^{(i)}] \Big/ \left[\Delta\kappa_{n+1}^{(i+1)} + \Delta\lambda_{n+1}^{(i+1)} \operatorname{tr}\left(\mathbf{C}^0 : \frac{\partial f}{\partial\boldsymbol{\sigma}}\right)_{n+1}^{(i)}\right]. \tag{A7}$$